Title: Optogenetic frequency scrambling of hippocampal theta oscillations dissociates working memory retrieval from hippocampal spatiotemporal codes

Authors: Guillaume Etter[1,*], Suzanne van der Veldt[1], Jisoo Choi[1], Sylvain Williams[1,*]

[1]McGill University & Douglas Mental Health University Institute, Montreal, Canada

* corresponding authors: sylvain.williams@mcgill.ca, 6875 Boulevard LaSalle, Verdun, QC H4H 1R3, Phone: 514 761-6131, Fax: 514 888-4067; etterguillaume@gmail.com

Abstract

The precise temporal coordination of activity in the brain is thought to be fundamental for memory encoding and retrieval. Pacemaker GABAergic neurons in the medial septum (MS) provide the largest source of innervation to the hippocampus and play a major role in controlling hippocampal theta (~8 Hz) oscillations. While pharmacological inhibition of the MS is known to disrupt memory, the exact role of MS inhibitory neurons and theta frequency rhythms in hippocampal representations and memory is not fully understood. Here, we dissociate the role of theta rhythms in spatiotemporal coding and memory using an all-optical interrogation and recording approach in freely behaving mice. We propose a novel paradigm to dissociate encoding of space, time and distance in freely moving mice and apply complementary optogenetic stimulation paradigms of MS GABAergic neurons to either pace or abolish theta altogether while recording large hippocampal cell assemblies using calcium imaging conjointly. We first show that optogenetic frequency scrambling of MS GABAergic neuron activity abolished theta rhythms and modulated the activity of a subpopulation of CA1 neurons. Such stimulation led to decreased memory retrieval in both a delayed non-match to sample task, a novel place object recognition task, as well as spontaneous cue-guided linear alternation. Strikingly, scrambled stimulations were not associated with disrupted encoding of place, time, distance, or multiplexed information. Our study suggests that theta rhythms play a specific and essential role in supporting working memory retrieval and maintenance while not being necessary for hippocampal spatiotemporal codes.

Introduction

The precise temporal coordination of neuronal activity is thought to be fundamental for memory encoding and retrieval. In particular, the medial septum (MS) has been proposed to act as the main zeitgeber to downstream structures[1]. It is a neurochemically heterogeneous structure composed of GABAergic[2], mainly parvalbumin (PV)-positive neurons[3], along with cholinergic[4] and a smaller population of glutamatergic neurons[5,6]. MS PV cells project directly onto GABAergic interneurons in the hippocampus giving rise to feedforward inhibitory control of hippocampal pyramidal cells[3]. Additionally, PV interneurons within the hippocampus are essential in pacing theta (~8 Hz) rhythms[7], and optogenetic stimulation of MS PV neurons directly[8,9] or of their terminals[10] in the hippocampus are associated with frequency-specific pacing of hippocampal oscillations whereas inhibition of the medial septum (MS) *in vivo* has been associated with reduced theta oscillations power[11,12].

While complete MS optogenetic inhibition has been associated with spatial memory impairments[13], these effects could potentially be attributed to disruption of cholinergic functions[14,15], which are known to be critical for memory function. The exact role of non-cholinergic MS PV cells in memory encoding and retrieval remains an active area of research and has only been described recently[16,17]. Importantly, the hippocampus plays an essential role in encoding and retrieval of episodic[19,20] and working[21] memory. Since the MS provides the largest subcortical inputs to the hippocampus and is essential in generating and maintaining theta rhythms, disruption of MS activity is likely to impact downstream hippocampal physiology and working memory[18]. Although the exact physiological mechanisms of hippocampus-dependent memory are currently unknown, it has been proposed that hippocampal place cells[22] that encode specific locations of a given context could support episodic memory[23]. In the hippocampal subfield CA1, spatial tuning relies at least in part on contextual sensory inputs[24]. Other variables such as time and distance can also be encoded

during visually guided locomotion[25,26] but also in the absence of sensory cues[27], likely using internal information including self-motion[28] (see Mehta[29] and McNaughton[30] for review). Representations of time and space can be represented conjunctively in hippocampal neurons, and such multiplexed spatiotemporal codes could be a candidate substrate for working memory[31–33]. In addition to clamping distal visual cues using a treadmill[34–36] or using virtual reality paradigms[25,26,37], spatiotemporal codes have also been extracted analytically using generalized linear models that implement space, time, and distance[36] although such approaches have not been employed extensively on recordings of neuronal activity during free exploration.

Several studies suggest that hippocampal theta rhythms could underlie temporal codes since theta rhythms tightly orchestrate hippocampal activity[38,39]. While time cells have also been reported in both CA1 and CA3 of rodents performing tasks that do not require working memory[40], pharmacological inhibition of the MS results in specific disruption of time but not place cells and is associated with decreased working memory[35]. An important drawback of pharmacological approaches is that they do not distinguish the relative contribution of GABAergic versus cholinergic cells to memory function[41], and inhibition of MS cholinergic activity was found to alter hippocampal spatial representations[42] and decrease working memory performance[43,44]. Surprisingly, pharmacological inhibition of the MS was associated with reduced theta oscillation power but not place fields[45], and this resilience of place cell activity during diminished theta was not due to experience-related plasticity mechanisms[46]. Previous attempts at inhibiting MS GABAergic interneurons specifically using optogenetics were associated with only a partial reduction, but not complete disruption of theta signals[47]. In turn, optogenetic pacing of theta oscillation has only been associated with minor changes in place cell characteristics, including a slight shift in firing frequency[9] and phase[48]. Additionally, while it is hypothesized that hippocampal temporal codes could be directly

controlled by MS inputs, causal evidence is still lacking. To this day, the exact role of MS-PV neurons in orchestrating hippocampal spatiotemporal codes and memory remains unknown.

Here we controlled MS PV activity using optogenetics to pace or abolish theta oscillations using a red-shifted excitatory opsin. We propose a novel approach to completely abolish hippocampal theta rhythms based on optogenetic frequency scrambling stimulations of MS neurons. Alternatively, pacing theta rhythms at their natural frequency in the same animals provides within-subject controls. We combined optogenetic control with calcium imaging of CA1 pyramidal cells in mice running on a linear track with sequential tones. In these conditions, we were able to separate place, time, and distance cells using an information theoretic approach. When performing optogenetic frequency scrambling of theta signals, both place and time representations were preserved and only a small subset of CA1 pyramidal cells were modulated by stimulation. We next found that ablation of theta oscillation was associated with impaired working memory retrieval suggesting that MS PV cells play a key role in generating hippocampal theta oscillations that are necessary for memory retrieval, but are not involved in spatiotemporal representations.

Results

CA1 pyramidal cells encode spatiotemporal information

To examine the spatiotemporal codes in large populations of CA1 principal cells, we injected a viral vector expressing $GCaMP6_{fast}$ under a CamKII promoter in the CA1 region of the hippocampus, implanted a GRIN lens above the injection site, and performed calcium imaging recordings of pyramidal neurons using open-source miniscopes[49,50] (fig. 1a,b; see supplemental fig. 1 for detailed histology). We extracted spatial footprints of neurons (fig. 1c)

and their corresponding calcium transients (fig. 1d) using CNMFe[51]. To tease apart the spatial and temporal tuning properties of principal cells, we developed a new task combining a linear track with three tone cues triggered by motion sensors at both ends of the track. A new tone was instantly triggered at the end of each run, informing the mice on its progression toward reward delivery. Every fourth run was cued with a high-pitched, continuous tone that was associated with the delivery of a reward at the end of the linear track (fig. 1e). The absolute location of each mouse, along with the time elapsed and distance traveled since the departure from the reward site were monitored (fig. 1f). Using these variables and binarized neuronal activity, we computed probabilistic tuning curves (fig. 1g) and derived mutual information (MI) between neuronal activity and location, time, as well as the distance for each recorded cell. In contrast to correlation-based analyses, MI does not assume linear, monotonic relationships between neuronal activity and behavioral variables but rather expresses the amount of uncertainty of one variable that can be explained by the other. The significance of MI values was tested using shuffled surrogates that underwent circular permutations (n = 1000) to preserve temporal dynamics of calcium transients. Neurons that encoded exclusively one variable with a MI greater than shuffled surrogates 99.5 of the time ($p < 0.05$) were labeled as either place-modulated (spatial), time-modulated (temporal), or distance-modulated (see Methods). For the following analyses, we focused on candidate cells that only encoded one significant variable (fig. 1h). Importantly, time-modulated cells were not systematically active at particular locations, and place-modulated cells were not systematically active at a given time (fig. 1i,j). While the majority of cells encoding a single variable were place-modulated, a large portion of neurons were conjunctive neurons that encoded more than one variable (17.98 ± 1.77 %). In contrast, cells encoding place exclusively represented 9.02 ± 1.61 % of the total recorded population, while 1.79 ± 0.68 % selectively encoded distance and

127 1.27 ± 0.09 % selectively encoded time (fig. 1k; additional examples of neurons tuned to time,
128 space, or distance along with their information content are shown in supplemental fig. 2).

129 Although our information theoretic approach can disentangle overlapping variables by
130 isolating cells that only significantly encode one variable, we further tested the relevance of
131 each cell type in encoding spatiotemporal variables using a naive Bayesian classifier to
132 decode location (fig. 1l-n), time elapsed (fig. 1o-q), and distance traveled (fig. 1r-t) on the
133 linear track[52]. We estimated the current state of each mouse by computing the maximum *a*
134 *posteriori* (MAP) value given neuronal activity and bootstrapped tuning curves computed
135 using either actual or circularly shuffled binarized activity (fig. 1l,o,r; see Methods for
136 detailed protocol). The quality of predictions was assessed using confusion matrices (fig.
137 1m,p,s) and by computing the euclidean distance between predicted state and actual state (fig.
138 1n,q,t). Importantly, our Bayesian decoder yielded an average error of 16.58 cm, which was
139 significantly lower than when decoding from shuffled surrogates (50.95 cm; t-test, $t_{98} = 127.3$,
140 $p < 0.0001$), and decoding using spatially modulated cells was significantly more accurate
141 than when using non-spatially modulated cells (t-test, $t_{98} = 29.43$, $p < 0.0001$; fig. 1n).
142 Similarly, the average decoding error for time elapsed was 6.45 s, which was significantly
143 lower than error computed using shuffled surrogates (19.12 s; t-test, $t_{98} = 101.5$, $p < 0.0001$).
144 Decoding using time-modulated cells yielded significantly better accuracy compared to non
145 time-modulated cells (t-test, $t_{98} = 10.63$, $p < 0.0001$; fig. 1q). Finally, average distance error
146 using our decoder was 61.40 cm, which was significantly lower than that of shuffled
147 surrogates (189.6 cm; t-test, $t_{98} = 141.1$, $p < 0.0001$). Decoding using distance-modulated cells
148 yielded significantly lower errors compared to non distance-modulated cells (t-test, $t_{98} = 9.58$,
149 $p < 0.0001$; fig. 1t).

150

Selective MS optogenetic control of theta oscillations

To examine the relative contribution of MS-generated theta signals to hippocampal spatiotemporal codes, we transfected the red-shifted excitatory opsin ChrimsonR in the MS (fig. 2a). In contrast to inhibitory opsins, ChrimsonR allowed us to either scramble or pace theta signals within subjects. Additionally, ChrimsonR is more effective than the more widely used Channelrhodopsin-2 and provides the capability to combine optogenetics with calcium imaging[53]. 14.91 ± 3.57 % of PV cells expressed ChrimsonR which we found sufficient to exert pervasive control over hippocampal oscillations (n = 4 mice; fig. 2b,c). In contrast, we found virtually no expression of ChrimsonR in ChAT cells (1.05 ± 1.052 % of ChAT cells also expressed ChrimsonR; fig. 2d,e).

We then implanted mice with fiber optics over the MS and performed 638 nm laser stimulation while recording local field potentials (LFP) in CA1 (fig. 2f). We found that MS scrambled and 8 Hz optogenetic stimulation could disrupt or pace theta oscillations, respectively (fig. 2g). While baseline natural theta displays some frequency variability in the 4-12 Hz frequency band, 8 Hz stimulations led to consistent and stable hippocampal oscillations at that frequency, whereas scrambled stimulations consistently abolished theta rhythms (fig. 2h). We found that oscillation strength (OS) in the theta band (see Methods) was significantly decreased by scrambled stimulations (0.45 ± 0.01 OS) compared to baseline epochs (0.67 ± 0.01 OS, $p < 0.0001$) and were not significantly different from OS of white noise control signal (0.50 ± 0.01 OS, p = 0.99). On the other hand, 8 Hz stimulations increased theta power significantly (0.82 ± 0.01 OS, $p < 0.0001$; n = 60 epochs) compared to scrambled stimulations. We also found a significant interaction between our stimulation patterns and LFP frequency band ($F_{10} = 6.467$, $p < 0.0001$). In particular, scrambled frequency stimulation significantly decreased theta power (0.341 ± 0.06 portion of baseline theta band power; p = 0.0394, pairwise t-test), while 8 Hz stimulations significantly increased theta

power (3.302 ± 0.76 portion of baseline theta band power, $p = 0.0004$, pairwise t-test; fig. 2j) leaving other frequency bands unaltered.

While our calcium imaging and electrophysiological analyses only included periods of locomotion (see Methods), we also found that we were able to reliably abolish (supplemental fig. 3a,b) or pace (supplemental fig. 3a,c) theta oscillations regardless of locomotor state (including periods of restfulness). While natural theta oscillation strength is correlated to locomotor speed (Pearson $R^2 = 0.059$, $p = 0.001$; supplemental fig. 3d), abolishing theta led to a loss of such correlation (Pearson $R^2 = 0.008$, $p = 0.223$; supplemental fig. 3e), as did 8 Hz stimulations (Pearson $R^2 = 0.0008$, $p = 0.714$; supplemental fig. 3f) suggesting that locomotor states did not override the effects of optogenetic stimulations on theta oscillations.

Hippocampal sharp-wave ripples (SWRs) play an essential role in memory consolidation[54–56] and stimulation of MS cholinergic neurons has been associated with reduced ripple activity[57] and impaired working memory[44]. While we found virtually no expression of ChrimsonR in MS cholinergic neurons, it was essential to measure the impact of our MS optogenetic stimulation on ripple physiology. To this end, we recorded CA1-LFP and performed 5s ON-OFF scrambled optogenetic stimulation in freely behaving mice exploring an open-field (supplemental fig. 4a). We measured attributes of ripple events before and during scrambled stimulation, and found no changes in power (t-test, $t_6 = 0.076$, $p = 0.941$; supplemental fig. 4b, left panel), frequency of occurrence (t-test, $t_6 = -1.688$, $p = 0.142$; supplemental fig. 4c, left panel), or width (t-test, $t_6 = 0.124$, $p = 0.905$; supplemental fig. 4d, left panel). Similarly, applying 8 Hz optogenetic stimulation had no discernable effects on ripple power (t-test, $t_6 = 0.378$, $p = 0.718$; supplemental fig. 4b, right panel), frequency (t-test, $t_6 = -1.643$, $p = 0.151$; supplemental fig. 4c, right panel), and width (t-test, $t_6 = -0.138$, $p = 0.894$; supplemental fig. 4d, right panel). Together with our histological results and previous reports that optogenetic stimulation of MS cholinergic neurons reduces the occurrence of

201 SWRs[57], our findings support the notion that these optogenetic stimulations are not affecting
202 cholinergic inputs to the hippocampus.

203

204 **Combining MS optogenetic stimulation and hippocampal calcium imaging**

205 To study the effects of theta manipulations on hippocampal spatial and temporal codes, we
206 combined MS optogenetic stimulation and calcium imaging in CA1. This experimental
207 paradigm raises two potentially important issues: GRIN lens implants involve tissue damage
208 that could alter the physiological state of theta oscillations, and the wavelength spectrum of
209 the excitation LED used to excite GCaMP6f could potentially overlap with that of the opsin
210 located on the terminal fibers of GABAergic MS fibers in the hippocampus.

211 To verify whether GRIN lens implants altered the physiology of theta, we first
212 implanted mice with a GRIN lens in the right hippocampus, with two electrodes in both left
213 and right hippocampi and found comparable theta signals in both hippocampi (fig. 3a). To
214 gain more statistical insights, we compared theta oscillations mice with electrodes only in the
215 right hippocampus, to mice with both a GRIN lens and an attached LFP electrode during open
216 field exploration, and found no significant differences between both groups (fig. 3b). We did
217 not find any significant difference between relative theta power to total LFP power of mice
218 implanted with a GRIN lens and LFP electrode (0.14 ± 0.007) versus an electrode only (0.154
219 ± 0.008; t-test, $t_{54} = 1.060$, $p = 0.29$).

220 Although previous reports have reported that combining optogenetic stimulation of
221 ChrimsonR in cell bodies with calcium imaging of neurons at the vicinity of terminals is
222 possible with minimal crosstalk[53], we next controlled for any potential opsin activation of MS
223 terminals in the hippocampus by recording CA1-LFP while emitting excitation light with our

224 miniscope through a GRIN lens in mice injected with ChrimsonR in the MS. After calibrating
225 miniscope light output power (fig. 3c), we found no effect of miniscopes blue excitation light
226 on endogenous theta power when using excitation light power below 0.5 mW/mm^2
227 (1ANOVA, $F_{(4,295)} = 0.7729$, $p = 0.5435$; fig. 3d). Since it has been reported that miniscope
228 excitation light can induce slight depolarization of terminals transfected with ChrimsonR[53],
229 thus hindering further optogenetic-induced depolarization, we next stimulated our control
230 mice while imaging with a ~0.3 mW/mm^2 miniscope LED power and were able to
231 significantly disrupt or pace theta using scrambled or 8 Hz stimulation respectively (Friedman
232 test $\chi^2 = 6$, $p = 0.0278$; fig. 3e).

233

234 **Disruption of theta rhythms modulates a small portion of CA1 cells**

235 We then performed phasic (5s ON, 5s OFF) optogenetic stimulations of MS while recording
236 CA1 pyramidal cells and as mice freely explored an open-field (fig. 4a). We found that a
237 portion of recorded cells were consistently excited in these conditions, while others were
238 inhibited (fig. 4b; see Methods). The activity of pyramidal cells during stimulation was
239 overall lower compared to baseline, for both scrambled stimulation during running (Pearson
240 correlation, $R^2 = 0.567.$, $p < 0.0001$) and rest ($R^2 = 0.521$, $p < 0.0001$) periods, as well as for 8
241 Hz stimulation ($R^2 = 0.6.$, $p < 0.0001$ for rest periods; $R^2 = 0.632.$, $p < 0.0001$ for running
242 periods; n = 1849 cells, N = 5 mice; fig. 4c). Overall, ~6.42 ± 0.52 % of total cells were
243 significantly modulated by scrambled optogenetic stimulation (fig. 4d). Among those
244 modulated cells, 50.56 ± 6.38 % were inhibited while 49.43 ± 6.38 % were excited during
245 scrambled stimulations (n = 1849 cells, N = 5 mice; fig. 4e).

246 We next analyzed the effects of optogenetic stimulation on spatial tuning of
247 hippocampal neurons as mice freely explored the open field. To this end we computed activity

248 rate maps by using either epochs within or outside of stimulation periods (for the baseline
249 condition, we included epochs that followed the same 5s ON, 5s OFF pattern used for actual
250 stimulation; fig. 4f). Stability was then computed as the correlation between rate maps
251 computed for baseline and stimulation epochs. In spite of the aforementioned changes of
252 overall activity, rate maps displayed no change of spatial stability for either scrambled or 8 hz
253 stimulations (Kruskal-Wallis $H_3 = 3.5$, $p = 0.1773$; fig. 4g).

254

255 **MS optogenetic stimulation alters behavior but not spatiotemporal codes**

256 To assess the effects of theta disruption on temporal and spatial codes, we monitored CA1
257 pyramidal neuron activity on the 3-tone linear track (fig. 5a). Here we leverage one of the
258 main advantages of calcium imaging, which is the ability to register recorded cells over
259 several days, while performing scrambled or 8 Hz stimulations on selected days (fig. 5b; fig.
260 5c, bottom panel). We focused our analysis on pairs of days with the same amount of time
261 (48h) between testing (fig. 5c, top panel). For each condition, we assessed the portion of total
262 cells significantly encoding one or several variables, and found no effect of either 8 Hz or
263 scrambled stimulation on spatial and temporal encoding (RM-ANOVA; $F_2 = 0.807$, $p = 0.453$
264 for the main effect of stimulations; $F_6 = 1.283$, $p = 0.285$ for the interaction between
265 stimulation and encoded variable, n = 5 mice; fig. 5d).

266 While the portion of cells did not change under stimulation conditions, we assessed
267 the effect of MS stimulation on place-, time-, and distance-modulated cells' tuning curves
268 stability. To this end, we tracked neurons across days (fig. 5c; see Methods) and computed
269 stability of place and time fields as the pairwise correlation between fields across 48h.
270 Because CA1 is known to display prominent remapping over days[58], we also used a pair of
271 days with no stimulation to compute a baseline stability score to be used as a reference (fig.

5e-g). We found no change in stability during MS stimulation for place-modulated cells (1ANOVA, $F_2 = 1.907$, $p = 0.1511$; fig. 5h), time-modulated cells (1ANOVA, $F_2 = 2.201$, $p = 0.113$; fig. 5i), and distance-modulated cells (1ANOVA, $F_2 = 0.6962$, $p = 0.5024$; fig. 5j). We also extended the same analysis to conjunctive neurons (i.e. neurons that can encode more than one variable; supplemental fig. 5a-f) and found no effects of optogenetic stimulations on the stability of conjunctive spatial (1ANOVA, $F_2 = 3.731$, $p = 0.0661$; supplemental fig. 5g), temporal (1ANOVA, $F_2 = 1.993$, $p = 0.8228$; supplemental fig. 5h), and distance cells (1ANOVA, $F_2 = 0.469$, $p = 0.6400$; supplemental fig. 5i).

We next assessed the quality of spatiotemporal codes using random bootstrap samples (n = 160 cells per sample, n = 50 bootstrap samples) of all recorded cells. Namely, we applied a naive Bayesian classifier to decode location (fig. 6a,b), time (fig. 6c,d), and distance traveled (fig. 6e,f). Decoded errors were systematically lower than shuffled surrogates, including during 8 Hz or scrambled stimulation for location (2ANOVA, $F_{5,1100} = 5095$, $p < 0.0001$; fig. 6a), time (2ANOVA, $F_{5,1100} = 2731$, $p < 0.0001$; fig. 6c), and distance (2ANOVA, $F_{5,1100} = 2671$, $p < 0.0001$; fig. 6e) indicating that spatiotemporal codes were preserved during stimulation. To gain statistical insights, we z-scored decoding error by using both the actual and shuffled results (see Methods) for a given day, for every mouse (N = 5 mice; fig. 6b,d,f). MS optogenetic control did not significantly alter encoding of location (1ANOVA, $F_{2,11} = 2.2332$, $p = 0.1432$; effect size $\eta^2 = 0.29$; fig. 6b), time (1ANOVA, $F_{2,11} = 0.4561$, $p = 0.6452$; effect size $\eta^2 = 0.07$; fig. 6d), or distance (1ANOVA, $F_{2,11} = 0.6102$, $p = 0.5606$; effect size $\eta^2 = 0.09$; fig. 6f).

In the behavioral paradigm used to analyze temporal modulation of neuronal activity, mice are water-scheduled and expected to collect rewards as quickly as possible. Based on this assumption, we quantified the number of returns to an empty reward site as errors, and computed the percentage of correct runs to total runs as a proxy for performance (fig. 6g). In

297 these conditions we found a significant effect of optogenetic stimulation on performance
298 across days (Friedman test $\chi^2 = 6.000$, $p = 0.0278$) and in particular a significant difference in
299 performance between during baseline (78.70 ± 2.45 %) and scrambled stimulation (44.44 ±
300 5.56 %; multiple comparison, $p = 0.0429$; N = 3 mice; fig. 6h). Only mice with a minimum of
301 12 runs were included in this analysis. Because of the limitations of this task (low cognitive
302 load and low number of mice tested), we next set out to assess the effect of MS optogenetic
303 stimulation in standardized behavioral tasks. Importantly, it was previously reported that
304 pacing theta oscillations could decrease locomotor speed and its variability[10]. To thoroughly
305 assess the specificity of MS optogenetic stimulation on memory, we performed additional
306 experiments to rule out the direct effects of the optogenetic stimulations on locomotor
307 velocity.

308 A subset of mice injected with ChrimsonR and implanted with fiber optics in the MS
309 as well as LFP electrodes in CA1 were allowed to explore an open-field freely while being
310 subjected to 5s ON, 5s OFF optogenetic stimulations (supplemental fig. 6a). Consistently, 8
311 Hz stimulation led to consistent pacing of hippocampal oscillations to that frequency
312 (supplemental fig. 6b). Those stimulations were not associated with any apparent change in
313 locomotor behavior (supplemental fig. 6c), including mean speed (t-test, $t_{116} = 0.4140$, $p =$
314 0.6796; supplemental fig. 6d) and speed coefficient of variation (CV; t-test, $t_{116} = 0.8296$, $p =$
315 0.4095, n = 59 stimulation epochs; supplemental fig. 6e). Similarly, scrambled stimulation
316 consistently led to abolished theta oscillations (supplemental fig. 6f) but no apparent changes
317 in locomotor behavior (supplemental fig. 6g), including mean speed (t-test, $t_{118} = 0.2268$, $p =$
318 0.8210; supplemental fig. 6h) and speed CV (t-test, $t_{118} = 1.838$, $p = 0.686$, n = 60 stimulation
319 epochs; supplemental fig. 6i).

320 While natural theta frequency and locomotor speed are correlated[59], the exact direction
321 of causation between these variables remains poorly understood. To answer this question, we

performed optogenetic stimulation using a 5s ON, 5s OFF paradigm and a random frequency was selected for each stimulation epoch (supplemental fig. 6j). These stimulation frequencies covered the entirety of the theta band spectrum (supplemental fig. 6k). As expected, we found that natural theta oscillations frequencies are directly correlated to running speed for one example mouse (R^2 = 0.1114, $p < 0.0001$; supplemental fig. 6l). Importantly, when theta oscillation frequency results from MS optogenetic control, the correlation drops below chance level (R^2 = 0.0006779, p = 0.6244; supplemental fig. 6m) suggesting that locomotion dictates theta frequency, but not the opposite. We systematically replicated these results across mice and observed a drop in the correlation between theta frequency and locomotor speed under optogenetic stimulation control (paired t-test, t_3 = 3.922, p = 0.0295; supplemental fig. 6n). Altogether, these results support that our optogenetic stimulation does not alter locomotor behavior, which is highly relevant for the next behavioral assays.

Disruption of theta signals impairs spatial recognition and working memory retrieval

To test the role of theta signals in spatial memory, we prepared a dedicated group of mice injected with ChrimsonR and implanted with a fiber optic in the MS (fig. 7a, left panel). Mice were subjected to a novel place object recognition (NPOR) task (fig. 7a, right panel). To assess the role of theta oscillations in memory encoding and retrieval, we performed optogenetic stimulations specifically during the sample and test phases and computed the recognition index (RI; see Methods). When stimulating during retrieval, memory performance was significantly reduced for both scrambled (0.472 ± 0.048 RI, n = 6 mice) and 8 Hz stimulations (0.435 ± 0.057 RI, n = 6 mice) groups, compared to YFP controls that displayed a significant increase in object exploration during testing (0.61 ± 0.018 RI, n = 12 mice; 2ANOVA, $F_{4,31}$ = 3.283 for the main effect of treatment, p = 0.0097; effect size for the main

effect of group, η^2_p = 0.306 fig. 7b). On the other hand, scrambled stimulations during encoding did not impair memory at test time (0.60 ± 0.034 RI, p = 0.0157, n = 6 mice) but 8 Hz stimulation during encoding lowered memory performance to chance levels (0.39 ± 0.074 RI, p = 0.8740, n = 6 mice,).

To further examine the effect of optogenetic control of the MS on specific phases of working memory function (encoding, maintenance, and retrieval), mice were transfected with ChrimsonR and implanted with fiber optics in the MS and trained in a delayed non-match to sample (DNMTS) task. In the sample phase, mice were forced to run to a randomly designated arm to collect a reward. After a delay (10 s), they could either run in the opposite arm (correct choice) to receive another reward, or run in the same, unrewarded arm (incorrect arm; fig. 7c). The advantage of this task is to allow for repetitive testing, specific isolation of task phases (training, delay, testing) and within-subject controls. Mice were trained in this task with no stimulation until criterion performance of 0.8 (portion of correct trials) was reached for at least two days. Both ChrimsonR and YFP control mice displayed significant improvement over time (RMANOVA, F_8 = 8.737, p < 0.0001 for the main effect of training days). Importantly, we found no learning rate differences between the two groups (pairwise Tukey; p = 0.42; fig. 7d). Once mice had learned the rule associated with the DNMTS task, we assessed performance while delivering either scrambled (0.792 ± 0.045) or 8 Hz (0.850 ± 0.036) optogenetic stimulation in the encoding phase (forced choice) only, and did not observe any difference in performance compared to baseline (0.825 ± 0.030, RM-ANOVA, F_{11} = 2.197, p = 0.547 , n = 12; fig. 7e). When stimulated only during the delay period, only scrambled stimulations significantly decreased memory performance (0.733 ± 0.057) compared to baseline (0.825 ± 0.030, RM-ANOVA, F_{11} = 3.483, p = 0.0495; effect size for the main effect of treatment, η^2_p = 0.109; fig. 7f). In contrast, when stimulated during retrieval, mice stimulated with 8 Hz displayed significantly reduced memory performance

371 (0.675 ± 0.049) compared to baseline (0.825 ± 0.030, RM-ANOVA, $F_{11} = 3.265$, $p = 0.050$;
372 fig. 7g). In contrast, YFP control mice were not affected by stimulations during encoding
373 (RM-ANOVA, $F_2 = 0.1314$, $p = 0.8781$), the delay period (RM-ANOVA, $F_2 = 0.2020$, $p =$
374 0.8197), or retrieval (RM-ANOVA, $F_2 = 0.0454$, $p = 0.9557$; effect size for the main effect of
375 treatment, $\eta^2_p = 0.196$) of working memory.

376 Surprisingly, 8 Hz optogenetic stimulations that are associated with pacing of theta
377 oscillations led to decreased performance when applied during either encoding or retrieval of
378 episodic memory in the NPOR task, as well as spatial working memory retrieval in the
379 DNMTS task. To further understand the effects of pacing theta on hippocampal physiology,
380 we analyzed phase locking of theta oscillation before and during 8 Hz optogenetic
381 stimulations (supplemental fig. 7a) and found that such stimulation led to a high phase
382 synchrony across stimulation epochs (supplemental fig. 7b). Furthermore, we analyzed the
383 cross-correlation of theta oscillation across dorsal CA1 (~1 mm distance between electrodes
384 along the septotemporal axis (supplemental fig. 7c) and found that pacing theta rhythms at 8
385 Hz led to increased cross correlation between those two electrodes (supplemental fig. 7d).

386

387 **Discussion**

388 Within the septohippocampal system, the exact causal relationships between (1) MS activity,
389 (2) hippocampal oscillations, (3) hippocampal neuron activity, and (4) behavior including
390 memory remain an active area of research. In particular, whether and how the MS supports
391 encoding of place and time in the hippocampus, as well as its specific contribution to memory
392 function remain unclear. Here, we leveraged more recent techniques that allowed us to record
393 >1000 neurons while performing optogenetic stimulation of MS neurons with a sub-second
394 resolution to control theta rhythms and assess its role in hippocampal physiology and

memory. Importantly, using an excitatory opsin and either scrambled or 8 Hz stimulations, we were able to consistently and robustly abolish or pace hippocampal theta respectively. Compared to MS inhibition using either an inhibitory opsin or pharmacological compounds (e.g. muscimol), our approach enables a within-subject comparison of two opposed states (paced vs abolished theta) while maintaining activity levels in MS-PV cells. We combined a novel tone-cued linear track task that, together with information theoretic approaches, allowed us to disentangle spatial and temporal hippocampal codes. This method alleviates the need for arbitrary thresholds, enabling a standardized approach to calcium imaging analysis as described previously[52]. While a large portion of CA1 pyramidal neurons expressed a mixture of spatiotemporal codes, we focused our analyses on neurons tuned specifically to place, time, or distance traveled.

While spatial coding has been extensively investigated in CA1, temporal and distance codes have recently gained more interest. Temporal[27,34–36] and distance[36] codes have been extracted by clamping visuospatial cues or extracted analytically using generalized linear models in virtual reality paradigms[25,26,37]. Here we propose a novel approach to disentangle spatial, temporal, and distance codes using an information theoretic approach which, together with our novel cued-alternation task, enables the analysis of real world spatiotemporal and multiplexed codes in freely moving animals. Strikingly, a large amount of CA1 pyramidal neurons encode multiplexed information of location, distance, and time as previously reported[25,26,37] in addition to self-motion signals such as acceleration, speed, and orientation[60].

Frequency scrambling and 8 Hz optogenetic stimulations drastically abolished or paced theta rhythms, respectively, and led to an overall decreased activity in a subpopulation of CA1 pyramidal cells while not causing significant changes in place cell activity, similar to previous reports using either pharmacological inhibition[35,45,46], or optogenetic[9,48] pacing of MS or septal inputs to the hippocampus. As MS neurons are known to be the primary driver of

420 hippocampal oscillations, we expected that MS stimulation would be associated with
421 disrupted time or distance cell activity in conditions of reduced theta rhythms, but did not
422 observe any change for both abolished and paced theta conditions. Additionally, pacing of
423 hippocampal oscillations to 8 Hz did not lead to changes in the quality of spatial codes as
424 reported previously[9], and did not alter temporal codes as observed in our behavioral paradigm.

425 While it was reported that time (but not place) cells could depend directly on medial
426 entorhinal cortex (MEC) inputs[61], other studies show that MEC lesions do not lead to any
427 alterations in hippocampal time cell physiology[62]. Notably, a more recent investigation found
428 that optogenetic pacing of the MS did not disrupt the spatial codes of grid cells in the
429 entorhinal cortex[63], further suggesting that MS activity is not directly involved in spatial codes
430 within the hippocampal formation. Together with our results, this indicates that temporal
431 codes could either be the result of MS-dependent computations within the entorhinal cortex[63]
432 (1), or be generated intrinsically within the hippocampus itself (2).

433 While early studies found that the MS played an essential role in maintaining time
434 cells and supporting working memory[35], recent experimental evidence shows that the exact
435 contribution of time cells to working memory performance could be less than previously
436 thought[62]. Since MS-PV neurons likely maintain significant activity levels during frequency
437 scrambling optogenetic stimulation (in contrast to inhibition approaches), our results strongly
438 support the role of precisely timed septal activity in supporting working memory, as
439 hypothesized previously[18]. Although we observed reduced memory performance when using
440 optogenetic stimulation during retrieval, stimulation during the encoding phase of the delayed
441 non-match to sample tasks was not associated with reduced memory in the DNMTS task.
442 Pacing theta oscillations at 8 Hz during either the encoding or retrieval phase of the NOPR
443 task led to impaired memory retrieval. Our electrophysiological analyses further reveal that
444 such stimulation caused distant regions of dorsal CA1 to be entrained at the same phase, with

non-physiological phase locking. While we did not directly investigate the causal relationship between phase changes and memory performance, phase locking of pyramidal neurons to theta oscillation has previously been shown to be a predictor of memory performance[64].

While we describe spatiotemporal codes in freely moving animals, one notable limitation of our approach to establish temporal and distance tuning properties is that it requires four times more sampling than a regular linear track which increases the chances of photobleaching when adding stimulation conditions to the experimental timeline. While we found that spatial codes remained unaffected by optogenetic stimulations within the same session, more recent imaging hardware that includes sensors with increased sensitivity could help prevent photobleaching and allow for longer recording sessions, and thus sampling of temporal and distance cells along with stimulations. We also found that the pool of neurons that significantly and specifically encode only one variable is small in comparison to the number of conjunctive neurons, making sampling requirements for these highly specific neurons much higher.

We provide experimental evidence that manipulation of MS does not alter locomotor speed and that conversely, locomotor speed does dictate theta frequency. Even though place and time codes were preserved during our MS stimulations, a portion (~6%) of cells were directly modulated, and could account for memory impairments observed in our behavioral assays. PV interneurons in the hippocampus have previously been reported to be part of a microcircuit essential in regulating memory consolidation[65,66], and our optogenetic manipulations could be associated with silencing of these cells to some extent. Moreover, although we did not observe changes in frequency bands other than theta, we cannot exclude that CA1 pyramidal neuron spike timing could be drastically altered when scrambling theta oscillations, while 8 Hz stimulation were shown to not result in increased hippocampal activity[17], which could explain the differential effects of those stimulation patterns on working

470 memory performance. The memory impairments we observed were likely non-cholinergic:
471 firstly, in our immunohistological experiments we found virtually no expression of
472 ChrimsonR in ChAT neurons of the MS. Secondly, our optogenetic stimulations were not
473 associated with changes in hippocampal ripples, while previous reports indicate that ChAT
474 neurons stimulation is associated with reduced ripple frequency[44,57]. ChrimsonR transfection
475 of MS VGLUT2 neurons is also unlikely, since activation of these neurons is associated with
476 direct increase in locomotor activity[67], which we did not observe. Although the precise
477 temporal arrangement of CA1 pyramidal spikes could explain, at least partially, the effects of
478 MS stimulation on memory, alternative mechanisms should be taken into consideration.
479 Notably, in addition to the hippocampus and the entorhinal cortex, MS PV neurons project to
480 the retrosplenial cortex[3], and could be responsible for some of the memory impairments
481 observed here.

482 In summary, using calcium imaging, optogenetics, and electrophysiology, we found
483 that theta rhythms can be paced or abolished using stimulation of the MS. Such stimulation
484 impaired episodic as well as working memory retrieval. These effects were non-cholinergic,
485 and did not disrupt hippocampal ripple activity. Finally, while a small fraction of hippocampal
486 neurons responded directly to optogenetic stimulation of the MS, place, time, and distance
487 cells were not disrupted by manipulations of theta oscillations. Together these results suggest
488 that while MS input to the hippocampus plays an essential role in memory, multiplexed codes
489 in CA1 pyramidal neurons might not be the direct substrate for such functions.

Methods

Animals

All procedures were approved by the McGill University Animal Care Committee and the Canadian Council on Animal Care (protocol 2015-7650). A total of n = 41 male and female (8-16 weeks old) parvalbumin-cre mice (Jackson Laboratory) were used in this study. Mice were housed individually on a 12-hour light/dark cycle at 22°C and 40% humidity with food and water ad libitum. All experiments were carried out during the light portion of the light/dark cycle.

Adeno-associated viral vectors

Adeno-associated virus AAV5.CamKII.GCaMP6f.WPRE.SV40 (Addgene # 100834, obtained from University of Pennsylvania Vector Core) was used in all calcium imaging experiments. Adeno-associated virus (AAV) of serotype *dj* (hybrid capsid created from 8 different AAV serotypes) AAVdj-hSyn-ChrimsonR-tdTomato were obtained from the Vector Core Facility at Oregon Health and Science University in Portland, Oregon. Although hSyn is a housekeeping gene, we did not observe transfection in cholinergic cells (see Results and fig. 2b-e). An eYFP construct without the ChrimsonR sequence was used as a control (termed YFP control in this manuscript).

Surgical procedures

Mice were anesthetized with isoflurane (5% induction, 0.5-1 % maintenance) and placed in a stereotaxic frame (David Kopf Instruments). Body temperature was maintained with a heating pad, eyes were hydrated with gel (Optixcare), and Carprofen (10 ml/kg) was administered subcutaneously. The skull was completely cleared of all connective tissue and small craniotomies were performed using a dental drill for subsequent injection or implant.

515

516 *Viral injections*

517 All viral injections were performed using a glass pipette connected to a Nanoject III
518 (Drummond) injector at a flow rate of 1 nL/second. 500 nl of AAVdj-hSyn-ChrimsonR-
519 tdTomato (or eYFP control) was delivered into the medial septum at a rate of 1 nL/s, at the
520 following coordinates based on reference mouse stereotaxic atlas[68] (distance from Bregma in
521 mm): anteroposterior (AP) 0.85, mediolateral (ML) 0, dorsoventral (DV) −4.50 using a 5º
522 angle in the ML plane. After surgery, animals were continuously monitored until recovery.

523

524 *Fiber optic implant*

525 Two weeks post-injection, mice were anesthetized for implantation following the same
526 surgical procedure. 200 μm diameter fiber optics with ceramic ferrule (Thor labs) were
527 implanted at the same coordinates. Implants were cemented in place using C&B-Metabond®
528 (Patterson dental, MN). Black nail polish was applied over the dental cement to block light
529 emission during optogenetic stimulation.

530

531 *Electrode implants*

532 An array of 7 tungsten microelectrodes (~1 MΩ impedance) was lowered in dorsal CA1
533 spanning through *stratum pyramidale* (pyr), *stratum radiatum* (rad) and *stratum lacunosum*
534 *moleculare* (lm). Screws placed in the bone above the frontal cortex and cerebellum served as
535 ground and reference, respectively. Following electrode, ground and reference placement,
536 dental cement was applied to secure the implant permanently to the skull.

Implant for calcium imaging

We injected the AAV5.CamKII.GCaMP6f virus (200 nL at 1 nl.s–1) in hippocampal CA1 using the following coordinates: anteroposterior (AP) −1.86 mm from bregma, mediolateral (ML) 1.5 mm, dorsoventral (DV) 1.5 mm. 2 weeks following the injection, the mouse was anesthetized with isoflurane and the skull was cleared. A ~2 mm diameter craniotomy was performed in the skull above the injection site. An anchor screw was placed on the posterior plate above the cerebellum. The dura was removed, and the portion of the cortex above the injection site was aspirated using a vacuum pump, until the corpus callosum was visible. These fiber bundles were then gently aspirated without applying pressure on the underlying hippocampus, and a 1.8 mm diameter gradient index (GRIN; Edmund Optics) lens was lowered at the following coordinates: AP −1.86 mm from bregma, ML 1.5 mm, DV 1.2 mm. The GRIN lens was permanently attached to the skull using C&B-Metabond (Patterson Dental), and Kwik-Sil (World Precision Instruments) silicone adhesive was placed on the GRIN to protect it. 4 weeks later, the silicone cap was removed and CA1 was imaged using a miniscope mounted with an aluminum base plate while the mouse was under light anesthesia (~0.5 % isoflurane) to allow the visualization of cell activity. When a satisfying field of view was found (large neuronal assembly, visible landmarks), the base plate was cemented above the GRIN lens, the miniscope was removed, and a plastic cap was placed on the base plate to protect the GRIN lens.

Simultaneous calcium imaging and electrophysiological recordings

To control for the effects of GRIN implants on theta physiology as well as cross-talk between miniscope and optogenetic excitation lights, we attached tungsten micro-electrodes to GRIN lenses. To this end, we placed GRIN lenses horizontally under a low-magnification microscope in a dust-free environment. A tungsten microelectrode was gently placed on the top-edge of the GRIN lens using a micromanipulator. We used the known diameter of the GRIN lens as a reference unit to estimate the desired protrusion of the electrode (~50µm, further assessed digitally after taking a microphotograph of the preparation) in accordance with our planned implantation coordinates. Small amounts (~50µL) of superglue were deposited on the top edge of the GRIN lens with the electrode in place, left to dry for ~10min, before applying the next layer of glue. 5 thin layers were used to maintain the electrode attached to the GRIN lens. After implantation of these GRIN-electrode assemblies using the protocol described above, the protruding wires were gently bent and hidden under a protective cap (1-1.5 cm high) retrieved from the pear of a manual suction pipette as a replacement for Kwik-Sil.

In vivo **behavioral procedures**

Habituation

Mice were habituated by being gently handled for ~5 min over the course of one week, with progressive habituation to the plugging procedure (fiber optic, baseplate, and electrophysiological pre-amplified tethers. Animals were then water-scheduled (2h access per day). Miniscope recordings were performed at 30 Hz for 15 minutes, with only one recording session per day to minimize photobleaching.

Miniscope recordings

583 Miniscopes (V3) were assembled using open-source instructions as described previously
584 (miniscope.org). Imaging data were acquired using a CMOS imaging sensor (Aptina,
585 MT9V032) and multiplexed through a lightweight coaxial cable. Data was acquired using a
586 data acquisition (DAQ) box connected via a USB host controller (Cypress, CYUSB3013).
587 Animal behavior was recorded using a consumer grade webcam (Logitech) mounted above
588 the environment. Calcium and behavioral data were recorded using miniscope.org open
589 source DAQ custom acquisition software. The DAQ simultaneously acquired behavioral and
590 cellular imaging streams at 30 Hz as uncompressed .avi files of 1000 frames, along with
591 timestamps to enable precise temporal alignment of behavioral and calcium imaging data.

592

593 *In vivo electrophysiological recordings*

594 Following 1 week of post-surgical recovery and one week of habituation to the tethering
595 setup, LFP from implanted mice was recorded. All recorded signals from implanted
596 electrodes were amplified by the tether pre-amplifier before being digitized at 22 KHz using a
597 digital recording system (Neuralynx, USA). Recordings of each channel signal were saved in
598 a dedicated file along with video recordings and TTL signals from the Laser Diode for
599 subsequent analysis.

600

601 *Optogenetic stimulation*

602 Laser stimulation was delivered through a fiber optic cord (200 μm diameter) using a laser
603 diode fiber light source (Doric Lenses). Light intensity was calibrated and wavelength-
604 corrected using the Power Meter Bundle with the PM100D Console and S130C Slim
605 Photodiode Sensorlight (Thorlabs). Every pacing stimulation (including 8 Hz) was performed

using 5 ms square pulses. To apply scrambled light stimulation, we used an Arduino microcontroller to generate a white noise oscillation signal directly fed into the analogue input of the laser diode driver. To perform randomly selected frequency stimulation, we used a standard 5s ON, 5s OFF protocol but for each stimulation epoch, we used an Arduino microcontroller to randomly select a stimulation frequency in the theta band. When applying optogenetic stimulation during behavior, a loose piece of heat shrink tubing was fitted around the junction between the patch cord and the mouse' ferrule implant to limit visible light emission. Light intensities are expressed as nominal power, as measured at the tip of the fiber optic implant - cord assembly, and corrected for the appropriate wavelength.

Behavioral assays

Sequential tone linear track

Mice were water scheduled and could access water only for 2h per day from 6-8 pm. To disentangle spatial, temporal, and distance codes, we build a 134 cm long linear track using medium gray Lego® bricks which allows easy modifications and implementations without the need to permanently modify the structure of the maze. Pyroelectric sensors were placed in each end of the linear track, and were connected to an Arduino microcontroller. Each detection triggered a new tone in sequence, indicating the progress to reward delivery. The following tones were used and delivered using a piezo speaker: 1Hz beeps at 2,000Hz, 4Hz beeps at 3,000Hz, and a continuous tone at 4,000Hz. When the last, continuous tone was triggered, a reward (10% sucrose in water) was delivered at the starting end of the linear track in the cap of a 15 mL Falcon tube. Changes in running direction before triggering the next tone were considered as errors and did not trigger reward delivery. Performance was measured as the number of correct runs (with no error) divided by the number of total runs.

Novel object place recognition

On the first day, mice were allowed to freely explore a 45x45 cm dark gray open-field that contained visual cues (large white horizontal and vertical gratings) on its walls for 10 min. On the second day, two identical objects (helping hand base) were presented for 10 min. On the third day, mice were allowed to explore the same open field while the location of one of the two objects was displaced. To control for potential spatial preference biases, both the initial as well as the displaced position of objects were randomized. Mice were attributed a random testing order that was kept identical throughout the three days of testing. Behavior was recorded with a video camera and analyzed offline. Behavioral analysis was performed blind to the genotype and treatment. Object explorations were defined as epochs where mice have their nose within 1 cm of an object. Recognition index (RI) was computed as the following:

$$RI = \frac{t_{novel}}{t_{novel} + t_{familiar¿}}$$

where t_{novel} and $t_{familiar}$ represent the time exploring novel and familiar objects, respectively. This metric can also be computed in the sample phase for the prospectively novel (displaced) object to assess potential pre-existing preferential biases.

Automated delayed non-match to sample task

Mice were water-scheduled and trained in a continuous T-maze to a delayed non-match to sample task. Briefly, each trial was divided into two phases: sample and test. In the sample phase, one arm was blocked and mice were forced to explore the opposite arm where they received a 50 μL of 10% sucrose water reward. After completing the sample phase, mice were

subjected to a delay (10 s). Then, during the test phase, both arms could be explored, but only the opposite (unexplored) arm is baited, so that mice have to alternate locations between sample and test phases. Mice were subjected to 10 trials (sample + test) per day, for 10 consecutive days, and the daily success rate was calculated at the number of correct choices divided by the total number of trials.

Post-mortem histological analyses

After completion of behavioral testing, mice were deeply anesthetized with a mixture ketamine/xylazine/acepromazide (100, 16, 3 mg/kg, respectively, intraperitoneal injection) and perfused transcardially with 4% paraformaldehyde (PFA) in PBS. Brains were extracted and postfixed overnight in PFA at 4 ºC and subsequently washed in PBS for an additional 24 h at 4 ºC. Brains and sections were cryoprotected in a solution of 30 % ethylene glycol, 30 % glycerol, and 40 % PBS until used. Each brain was then sectioned at 50 µm using a vibratome: every section was sequentially collected in 4 different 1.5 mL tubes to allow different analyses (electrode location, immunohistochemistry).

Immunohistology

Using one tube of collected brain sections (25% sampling) for each analysis, sections were washed 3x5 min in PBS to remove cryoprotective solution. Sections were first incubated overnight with PGT (0.45 % Gelatin and 0.25 % Triton in PBS) at 4 ºC. Next, slices were incubated with primary antibodies: either 1:200 goat anti-choline-acetyl-transferase from Millipore or 1:500 mouse anti-parvalbumin monoclonal IgG1 from Sigma-Aldrich in PGT at room temperature for 48 h or 2 h respectively. Following washes of 10, 20, and 30 min,

676 sections were then incubated with secondary antibodies [1:2000 donkey anti-goat coupled
677 with Alexa 488 or 1:500 goat anti-mouse IgG1 coupled to Alexa 488 (Life Technologies)] in
678 PGT for 45 min. Following 10, 20, and 30 min washes, sections were then mounted on glass
679 slides and permanently coverslipped with Fluoromount mounting medium that contained
680 DAPI. Only mice with histologically confirmed placement of implants were included in this
681 study. For GRIN lenses, the surface of the lens had to be < 100µm above *stratum pyramidale*
682 and GCaMPf expression was confirmed using fluorescence microscopy. Electrophysiological
683 implants had to include at least one microelectrode in CA1 *stratum radiatum* or *stratum*
684 *pyramidale*. Finally, the tips of fiber optics had to be within 100 µm of the medial septum
685 region, and proper construct expression was assessed using fluorescence microscopy.

686

687 **Data analysis**

688 Except for analyses of sharp-wave ripples and explicit impact of locomotion on physiological
689 recordings, electrophysiological and calcium imaging analyses were performed only on
690 periods of locomotion (>2 $cm.s^{-1}$ in the open field; >5 $cm.s^{-1}$ on the linear track).

691

692 *Automatized tracking of behavior*

693 To extract information about the position, velocity, and head direction of mice, we used
694 DeepLabCut[69,70]. Briefly, we trained a model to detect mice ears, nose, body, and tailbase.
695 Head direction was estimated using the angle between either each ear or the nose and body
696 depending on measurement availability. Location data was interpolated to calcium imaging
697 sampling frequency using linear interpolation. Velocity was extracted by computing $\Delta d/\Delta t$
698 where d is the distance and t time, and subsequently smoothed the result by applying a

gaussian filter with sigma = 33 ms to remove movement artifacts. Velocity signals were used to identify periods of locomotor activity, using a threshold of 5 $cm.s^{-1}$, and used selectively to compute place, time, and distance modulation of activity.

Calcium imaging analysis

Calcium imaging data analysis was performed using MATLAB 2020a and Python 3.8.4. Video recordings were analyzed using the Miniscope Analysis pipeline (https://github.com/etterguillaume/MiniscopeAnalysis). Briefly, rigid (rotation and translation) motion correction was applied using NoRMCorre[71], and videos were spatially downsampled (3x) before concatenation. Calcium traces were extracted using CNMFe[51] using the following parameters: gSig = 3 pixels (width of gaussian kernel), gSiz = 20 pixels (approximate neuron diameter), background_model = 'ring', spatial_algorithm = 'hals', min_corr = 0.8 (minimum pixel correlation threshold), min_PNR = 8 (minimum peak-to-noise ratio threshold).

Raw calcium traces were filtered to remove high-frequency fluctuations and binarized: briefly, neurons were considered active when normalized calcium signal amplitude > 2 standard-deviations, and first-order derivative > 0 (see Etter et al., 2020 for additional details on the methodology[52]). To extract neurons tuning to specific variables, location, time, and distance were binned (location: 3 cm bins; time: 1 s bins; distance: 3 cm bins). From binarized signals, we computed the marginal likelihood of cells being active $P(A)$ that we use as a proxy for neuronal activity. More importantly, we then derive activity likelihood, or the 'probability of being active given the state of a variable' $P(A|S_i)$ using binned variables:

$$P(A|S_i) = \frac{time\ active\ while \in bin\ i}{time \in state}$$

where A is the activity level (0 or 1) of a given neuron, when being in bin i of a given state S. These values were smoothed using a Gaussian kernel with $\boldsymbol{\sigma}$ = 5, 10, or 15 for spatial, temporal, and distance tuning curves respectively.

To identify place, time, and distance cells, we computed the mutual information (MI) between neuronal activity and the bin i of a given state S using the following:

$$MI = \sum_{i=1}^{M} \sum_{j=1}^{2} P(S_i \cap A_j)\, x \log 2 \left(P \frac{(S_i \cap A_j)}{P(S_i)\, x P(A_j)}\right)$$

where M is the total number of possible behavioral states, $P(S_i \cap A_j)$ is the joint probability of the animal being in bin i concurrently with activity level j (0 or 1). To assess the significance of the obtained MI value, we then generated n = 1000 shuffled surrogates using random circular permutations. We chose circular permutations because they remove the temporal relationship between neuronal activity and behavior, while still preserving the temporal structure of calcium transients and therefore leads to more conservative results (as opposed to complete randomization of every data point, which inflates the significance value of results). Because shuffled surrogates were not systematically normally distributed, we used a non-parametric approach where the p-value (p_N) corresponds to the number of datapoints from the shuffled distribution that are greater than the actual data for each bin, divided by the number of permutations[52,72].

To determine the modulation of cells by optogenetic stimulations, we used a similar approach but computed the MI between neuronal activity and the binarized stimulation signals (thus treated as a behavioral state). The same circular shuffling procedure was then used to extract statistical significance.

Naive Bayes decoder

To further evaluate the significance of neuronal activity at the population level, we trained a naive Bayesian decoder with a uniform prior to predict spatiotemporal variables from binarized neuronal activity. The posterior probability density function, which is the probability that an animal is in a particular bin S_i, given the neural activity A is calculated using the following equation:

$$P(S_i|A)=\frac{P(A|S_i)\,x\,P(S_i)}{P(A)}$$

where P(S|A) is the posterior probability distribution of states given neuronal activity. Using only epochs with velocity > 5 cm/s, a training dataset was generated using 90% of the data. The remaining 10% of the data was used for testing. Decoding error was calculated using 50 bootstrapped surrogates and a pool of 160 cells using randomly chosen data points with replacement. Every neuron is assumed to be independent of each other, which in practice is not the case and leads to greater reconstruction errors, but decreases computational time. The population posterior probability was derived from the following equation:

$$P(S|A)=\prod_{k=1}^{N}\frac{P(A_k|S)\,x\,P(S)}{P(A_k)}$$

with N corresponding to the number of neurons used. Finally, the decoded data point corresponds to the maximum *a posteriori* (MAP):

$$\hat{y}=arg\,max\exp\left[\sum_{k=1}^{N}\log\left(1+\frac{P(A_k|S)\times P(S)}{P(A_k)}\right)-1\right]$$

The exponential-logarithm trick is used to prevent underflow when multiplying a large number of small probabilities, which is a correct approximation since the posterior is a smooth convex function.

Temporal filtering was applied to posterior probabilities using:

$$P(S|A_k(t))=\prod_{k=1}^{N}\prod_{t=1}^{T}\frac{P(A_k(t)|S)\times P(S)}{P(A_k(t))}$$

where t is a given timestep, and $P(S|A_k(t))$ the *a posteriori* distribution of states at timestep t for neuron k. The number of past timesteps used to estimate the mouse state at time t is determined by T, which we set as 2 s unless noted otherwise. On the linear track, decoding error was assessed as:

$$decoding\,error = |decoded\,state - actual\,state|$$

In order to compare decoding scores across animals, we z-scored decoding errors using the following equation:

$$z = \frac{\bar{x} - \bar{s}}{\sigma(x)}$$

where $\bar{x}$ is the average actual decoding error, $\bar{s}$ is the average decoding error using shuffled surrogates, and $\sigma(x)$ is the standard deviation of the actual decoding error.

Tracking cells over multiple days

Neurons were tracked over multiple days using a probabilistic method as previously described[73]. Briefly, spatial footprints were aligned using rigid alignment to correct for rotations and translations. After alignment, we considered candidate sets of cells to be the same neuron if their maximal distance was < 12 um, and used the modeled spatial correlation threshold (usually in the range .6 - .8) to determine the identity of cell pairs across days. Finally, we assessed the stability of the spatial representation using pairwise field correlation (Pearson correlation of tuning curves).

Electrophysiological analysis

Electrophysiological data analysis was performed using MATLAB 2020a and both the signal processing as well as the wavelet toolbox. Wavelet convolution was applied to LFP signals using complex Morlet wavelets ('cmor1-1.5' in MATLAB) when both time- and frequency-domain accuracy was required. Moving window Fourier convolution (2 s window in the theta band, 5 s window in the gamma band, 10 ms moving steps) was used when frequency-domain accuracy was privileged over time-domain accuracy (e.g. to plot dominant frequency when pacing using optogenetics). Analysis of power spectral densities was performed when mice were running at 5 $cm.s^{-1}$ or above, unless described otherwise.

Oscillation strength

Oscillation strength was computed as the ratio of cumulative power spectral density around the peak oscillation frequency ± 1 Hz to the cumulative band power in the theta (4 - 12 Hz) band. This metric becomes 1 when all power spectral density falls within the peak oscillation frequency (e.g. 8 Hz if stimulating at that frequency).

Sharp-wave ripples detection and analysis

To monitor sharp-wave ripples (SWRs), mice were allowed to freely explore an open-field for 10 min while recording. Stimulations (scrambled or 8 Hz) were performed with a 5s ON, 5s paradigm. Only periods of quiet restfulness were considered for analysis. To this end, we computed the z-scored ratio of theta/delta power after filtering for each frequency band and performing a Hilbert transform, as described previously[74], and only considered periods where the resulting value was under 0. To detect SWRs, we filtered LFP signals in the 150-250 Hz frequency band and subsequently z-scored. Ripples were detected using the findpeaks

function in MATLAB, with the following parameters: threshold=4 sd, minpeakwidth=0 s, minpeakdistance=0.03 s.

Statistics

Unless stated otherwise, all data are presented as mean ± standard error of the mean (SEM) and statistical test details are described in the corresponding results. The distribution normality of each group was assessed using Shapiro-Wilk normality test and parametric tests were used only when distributions were found normal (non-parametric tests are described where applicable). 1ANOVA: one-way ANOVA; 2ANOVA: two-way ANOVA; RM-ANOVA: repeated measure ANOVA. $p < 0.05$ was considered statistically significant. *, $p < 0.05$; **, $p < 0.01$; ***, $p < 0.001$, ****, $p < 0.0001$. Effect size of 1ANOVA was assessed with η^2 using sum of squares (SS):

$$\eta^2 = \frac{SS_{between}}{SS_{total}}$$

Effect size of 2ANOVA and RM-ANOVA was assessed with partial η^2 using:

$$\eta^2_p = \frac{SS_{effect}}{SS_{effect} + SS_{error}}$$

Author information

Affiliations

McGill University & Douglas Mental Health University Institute, Montreal, Canada

Corresponding authors: sylvain.williams@mcgill.ca, etterguillaume@gmail.com

6875 Boulevard LaSalle, Verdun, QC H4H 1R3, Phone : 514 761-6131, Fax: 514 888-4067

Contributions

GE and SW designed the study. GE performed and analyzed *in vivo* experiments. SVDV performed and analyzed both behavioral as well as immunohistological experiments. JC performed surgeries for the mice used for controlling cross-talk between calcium imaging and optogenetics. GE and SW wrote the manuscript with inputs from all collaborators.

Competing interests

The authors declare no competing interests.

Correspondence author

Correspondence should be addressed to Sylvain Williams: sylvain.williams@mcgill.ca

Acknowledgements: We thank Ke Cui for helping to maintain the colony and perfusing mice; Mark P Brandon, Alexandra Keinath, and Eric Carmichael for comments on the manuscript.

Funding

This work was supported by funding from the Canadian Institutes for Health Research (CIHR) Foundation Program FDN-148478, the Natural Sciences and Engineering Research Council of Canada (NSERC) Discovery Grant RGPIN-2020-06717, and a Tier 1 Canada Research Chair to SW. SVDV was supported by a Vanier Canada Graduate Scholarship and the Richard H. Tomlinson Doctoral Fellowship. JC was supported by a Healthy Brains, Healthy Lives (HBHL) Graduate Student Fellowship and a McGill Integrated Program in

Neuroscience (IPN) Internal Student Award. The funders had no role in study design, data collection and analysis, decision to publish, or preparation of the manuscript.

Data availability

The data that support the findings of this study are available from the corresponding author upon reasonable request.

Code availability

All source codes used in the current study are available along with instructions here: https://github.com/etterguillaume/etter_et_al_2022

References

1. Colgin, L. L. Rhythms of the hippocampal network. *Nat. Rev. Neurosci.* **17**, 239–249 (2016).
2. Tóth, K., Freund, T. F. & Miles, R. Disinhibition of rat hippocampal pyramidal cells by GABAergic afferents from the septum. *J. Physiol.* **500**, 463–474 (1997).
3. Unal, G., Joshi, A., Viney, T. J., Kis, V. & Somogyi, P. Synaptic targets of medial septal projections in the hippocampus and extrahippocampal cortices of the mouse. *J. Neurosci.* **35**, 15812–15826 (2015).
4. Simon, A. P., Poindessous-Jazat, F., Dutar, P., Epelbaum, J. & Bassant, M.-H. Firing properties of anatomically identified neurons in the medial septum of anesthetized and unanesthetized restrained rats. *J. Neurosci.* **26**, 9038–9046 (2006).
5. Sotty, F. *et al.* Distinct electrophysiological properties of glutamatergic, cholinergic and GABAergic rat septohippocampal neurons: novel implications for hippocampal rhythmicity. *J. Physiol.* **551**, 927–943 (2003).
6. Manseau, F., Danik, M. & Williams, S. A functional glutamatergic neurone network in the medial septum and diagonal band area. *J. Physiol.* **566**, 865–884 (2005).
7. Amilhon, B. *et al.* Parvalbumin interneurons of hippocampus tune population activity at theta frequency. *Neuron* **86**, 1277–1289 (2015).
8. Etter, G. *et al.* Optogenetic gamma stimulation rescues memory impairments in an Alzheimer's disease mouse model. *Nat. Commun.* **10**, 1–11 (2019).
9. Zutshi, I. *et al.* Hippocampal neural circuits respond to optogenetic pacing of theta frequencies by generating accelerated oscillation frequencies. *Curr. Biol.* **28**, 1179-1188.e3 (2018).
10. Bender, F. *et al.* Theta oscillations regulate the speed of locomotion via a hippocampus to lateral septum pathway. *Nat. Commun.* **6**, 8521 (2015).
11. Green, J. D. & Arduini, A. A. Hippocampal electrical activity in arousal. *J. Neurophysiol.* **17**, 533–557 (1954).
12. Mitchell, S. J., Rawlins, J. N., Steward, O. & Olton, D. S. Medial septal area lesions disrupt theta rhythm and cholinergic staining in medial entorhinal cortex and produce impaired radial arm

maze behavior in rats. *J. Neurosci.* **2**, 292–302 (1982).

13. Gemzik, Z. M., Donahue, M. M. & Griffin, A. L. Optogenetic suppression of the medial septum impairs working memory maintenance. *Learn. Mem.* **28**, 361–370 (2021).

14. Knox, D. & Keller, S. M. Cholinergic neuronal lesions in the medial septum and vertical limb of the diagonal bands of Broca induce contextual fear memory generalization and impair acquisition of fear extinction. *Hippocampus* **26**, 718–726 (2016).

15. Jeong, D. U. *et al.* Improvements in memory after medial septum stimulation are associated with changes in hippocampal cholinergic activity and neurogenesis. *BioMed Res. Int.* **2014**, e568587 (2014).

16. Sans-Dublanc, A. *et al.* Septal GABAergic inputs to CA1 govern contextual memory retrieval. *Sci. Adv.* **6**, eaba5003 (2020).

17. Quirk, C. R. *et al.* Precisely timed theta oscillations are selectively required during the encoding phase of memory. *Nat. Neurosci.* **24**, 1614–1627 (2021).

18. Mehta, M. R. Role of Rhythms in Facilitating Short-Term Memory. *Neuron* **45**, 7–9 (2005).

19. Scoville, W. B. & Milner, B. Loss of recent memory after bilateral hippocampal lesions. *J Neurol Neurosurg Psychiat* **20**, 11–21 (1957).

20. Penfield, W. & Milner, B. Memory deficit produced by bilateral lesions in the hippocampal zone. *AMA Arch. Neurol. Psychiatry* **79**, 475–497 (1958).

21. Jeneson, A. & Squire, L. R. Working memory, long-term memory, and medial temporal lobe function. *Learn. Mem.* **19**, 15–25 (2012).

22. O'Keefe, J. & Dostrovsky, J. The hippocampus as a spatial map. Preliminary evidence from unit activity in the freely-moving rat. *Brain Res.* **34**, 171–175 (1971).

23. Robinson, N. T. M. *et al.* Targeted Activation of Hippocampal Place Cells Drives Memory-Guided Spatial Behavior. *Cell* **183**, 1586-1599.e10 (2020).

24. Muller, R. U. & Kubie, J. L. The effects of changes in the environment on the spatial firing of hippocampal complex-spike cells. *J. Neurosci.* **7**, 1951–1968 (1987).

25. Ravassard, P. *et al.* Multisensory Control of Hippocampal Spatiotemporal Selectivity. *Science* **340**, 1342–1346 (2013).

26. Aghajan, Z. M. *et al.* Impaired spatial selectivity and intact phase precession in two-dimensional virtual reality. *Nat. Neurosci.* **18**, 121–128 (2015).

27. Villette, V., Malvache, A., Tressard, T., Dupuy, N. & Cossart, R. Internally recurring hippocampal sequences as a population template of spatiotemporal information. *Neuron* **88**, 357–366 (2015).

28. Samsonovich, a & McNaughton, B. L. Path integration and cognitive mapping in a continuous attractor neural network model. *J. Neurosci. Off. J. Soc. Neurosci.* **17**, 5900–20 (1997).

29. Mehta, M. R. From synaptic plasticity to spatial maps and sequence learning: Place Field Plasticity. *Hippocampus* **25**, 756–762 (2015).

30. McNaughton, B. L., Battaglia, F. P., Jensen, O., Moser, E. I. & Moser, M.-B. Path integration and the neural basis of the 'cognitive map'. *Nat. Rev. Neurosci.* **7**, 663–78 (2006).

31. Eichenbaum, H. Time cells in the hippocampus: a new dimension for mapping memories. *Nat. Rev. Neurosci.* **15**, 732–744 (2014).

32. Eichenbaum, H. On the Integration of Space, Time, and Memory. *Neuron* **95**, 1007–1018 (2017).

33. Eichenbaum, H. The role of the hippocampus in navigation is memory. *J. Neurophysiol.* **117**, 1785–1796 (2017).

34. Pastalkova, E. Internally Generated Cell Assembly Sequences in the Rat Hippocampus Eva Pastalkova. **1322**, (2012).

35. Wang, Y., Romani, S., Lustig, B., Leonardo, A. & Pastalkova, E. Theta sequences are essential for internally generated hippocampal firing fields. *Nat. Neurosci.* **18**, 282–288 (2015).

36. Kraus, B. J., Robinson, R. J., White, J. A., Eichenbaum, H. & Hasselmo, M. E. Hippocampal 'time cells': time versus path integration. *Neuron* **78**, 1090–1101 (2013).

37. Moore, J. J., Cushman, J. D., Acharya, L., Popeney, B. & Mehta, M. R. Linking hippocampal multiplexed tuning, Hebbian plasticity and navigation. *Nature* **599**, 442–448 (2021).

38. O'Keefe, J. & Recce, M. L. Phase relationship between hippocampal place units and the EEG theta rhythm. *Hippocampus* **3**, 317–330 (1993).

39. Skaggs, W. E., McNaughton, B. L., Wilson, M. A. & Barnes, C. A. Theta phase precession in

hippocampal neuronal populations and the compression of temporal sequences. *Hippocampus* **6**, 149–172 (1996).

40. Salz, X. D. M. *et al.* Time cells in hippocampal area ca3. **36**, 7476–7484 (2016).

41. Givens, B. S. & Olton, D. S. Cholinergic and GABAergic modulation of medial septal area: Effect on working memory. *Behav. Neurosci.* **104**, 849–855 (1990).

42. Ikonen, S., McMahan, R., Gallagher, M., Eichenbaum, H. & Tanila, H. Cholinergic system regulation of spatial representation by the hippocampus. *Hippocampus* **12**, 386–397 (2002).

43. Givens, B. S., Olton, D. S. & Crawley, J. N. Galanin in the medial septal area impairs working memory. *Brain Res.* **582**, 71–77 (1992).

44. Zhang, Y. *et al.* Cholinergic suppression of hippocampal sharp-wave ripples impairs working memory. *Proc. Natl. Acad. Sci.* **118**, (2021).

45. Koenig, J., Linder, A. N., Leutgeb, J. K. & Leutgeb, S. The spatial periodicity of grid cells is not sustained during reduced theta oscillations. *Science* **332**, 592–595 (2011).

46. Brandon, M. P., Koenig, J., Leutgeb, J. K. & Leutgeb, S. New and distinct hippocampal place codes are generated in a new environment during septal inactivation. *Neuron* **82**, 789–796 (2014).

47. Boyce, R., Glasgow, S. D., Williams, S. & Adamantidis, A. Sleep research: Causal evidence for the role of REM sleep theta rhythm in contextual memory consolidation. *Science* **352**, 812–816 (2016).

48. Mouchati, P. R., Kloc, M. L., Holmes, G. L., White, S. L. & Barry, J. M. Optogenetic "low-theta" pacing of the septohippocampal circuit is sufficient for spatial goal finding and is influenced by behavioral state and cognitive demand. *Hippocampus* (2020) doi:10.1002/hipo.23248.

49. Aharoni, D. & Hoogland, T. M. Circuit investigations with open-source miniaturized microscopes: past, present and future. *Front. Cell. Neurosci.* **13**, (2019).

50. Ghosh, K. K. *et al.* Miniaturized integration of a fluorescence microscope. *Nat. Methods* **8**, 871–878 (2011).

51. Zhou, P. *et al.* Efficient and accurate extraction of in vivo calcium signals from microendoscopic video data. *eLife* **7**, e28728 (2018).

52. Etter, G., Manseau, F. & Williams, S. A probabilistic framework for decoding behavior from

in vivo calcium imaging data. *Front. Neural Circuits* **14**, (2020).

53. Stamatakis, A. M. *et al.* Simultaneous optogenetics and cellular resolution calcium imaging during active behavior using a miniaturized microscope. *Front. Neurosci.* **12**, 1–16 (2018).

54. Buzsáki, G. Hippocampal sharp wave-ripple: A cognitive biomarker for episodic memory and planning. *Hippocampus* **25**, 1073–1188 (2015).

55. Roux, L., Hu, B., Eichler, R., Stark, E. & Buzsáki, G. Sharp wave ripples during learning stabilize the hippocampal spatial map. *Nat. Neurosci.* **20**, 845–853 (2017).

56. Fernández-Ruiz, A. *et al.* Long-duration hippocampal sharp wave ripples improve memory. *Science* **364**, 1082–1086 (2019).

57. Vandecasteele, M. *et al.* Optogenetic activation of septal cholinergic neurons suppresses sharp wave ripples and enhances theta oscillations in the hippocampus. *Proc. Natl. Acad. Sci. U. S. A.* **111**, (2014).

58. Ziv, Y. *et al.* Long-term dynamics of CA1 hippocampal place codes. *Nat. Publ. Group* **16**, 264–266 (2013).

59. Sławińska, U. & Kasicki, S. The frequency of rat's hippocampal theta rhythm is related to the speed of locomotion. *Brain Res.* **796**, 327–331 (1998).

60. Veldt, S. van der, Etter, G., Mosser, C.-A., Manseau, F. & Williams, S. Conjunctive spatial and self-motion codes are topographically organized in the GABAergic cells of the lateral septum. *PLOS Biol.* **19**, e3001383 (2021).

61. Robinson, N. T. M. *et al.* Medial entorhinal cortex selectively supports temporal coding by hippocampal neurons. *Neuron* **94**, 677-688.e6 (2017).

62. Sabariego, M. *et al.* Time cells in the hippocampus are neither dependent on medial entorhinal cortex inputs nor necessary for spatial working memory. *Neuron* **102**, 1235-1248.e5 (2019).

63. Lepperød, M. E. *et al.* Optogenetic pacing of medial septum parvalbumin-positive cells disrupts temporal but not spatial firing in grid cells. *Sci. Adv.* **7**, eabd5684.

64. Rutishauser, U., Ross, I. B., Mamelak, A. N. & Schuman, E. M. Human memory strength is predicted by theta-frequency phase-locking of single neurons. *Nature* **464**, 903–907 (2010).

65. Xia, F. *et al.* Parvalbumin-positive interneurons mediate neocortical-hippocampal interactions

that are necessary for memory consolidation. *eLife* **6**, 1–25 (2017).

66. Donato, F., Rompani, S. B. & Caroni, P. Parvalbumin-expressing basket-cell network plasticity induced by experience regulates adult learning. *Nature* **504**, 272–276 (2013).

67. Fuhrmann, F. *et al.* Locomotion, theta oscillations, and the speed-correlated firing of hippocampal neurons are controlled by a medial septal glutamatergic circuit. *Neuron* **86**, 1253–1264 (2015).

68. Paxinos, G. & Watson, C. The rat brain in stereotaxic coordinates. *Acad. Press Inc* 439 (1997) doi:10.1016/0166-2236(87)90017-8.

69. Mathis, A. *et al.* DeepLabCut: markerless pose estimation of user-defined body parts with deep learning. *Nat. Neurosci.* **21**, 1281–1289 (2018).

70. Nath, T. *et al.* Using DeepLabCut for 3D markerless pose estimation across species and behaviors. *Nat. Protoc.* **14**, 2152–2176 (2019).

71. Pnevmatikakis, E. A. & Giovannucci, A. NoRMCorre: An online algorithm for piecewise rigid motion correction of calcium imaging data. *J. Neurosci. Methods* **291**, 83–94 (2017).

72. Cohen, M. X. *Analyzing neural time series data: theory and practice*. (The MIT Press, 2014).

73. Sheintuch, L. *et al.* Tracking the same neurons across multiple days in ca2+ imaging data. *Cell Rep.* **21**, 1102–1115 (2017).

74. Wikenheiser, A. M. & Redish, A. D. The balance of forward and backward hippocampal sequences shifts across behavioral states. *Hippocampus* **23**, 22–29 (2013).

1032 **Figure 1. Spatial and temporal codes are present in partially overlapping populations of**
1033 **CA1 neurons. a**, mice were injected with GCaMP6f in hippocampal subfield CA1 and
1034 subsequently implanted with a GRIN lens over the pyramidal cell layer for miniscope
1035 imaging. **b**, post-mortem coronal section from one example mouse. blue, DAPI; green,
1036 GCaMP6f. **c**, planar projection of extracted spatial footprints from one example mouse. **d**,
1037 corresponding calcium transients from a portion of recorded cells. **e**, behavioral paradigm
1038 used to disentangle time, place, and distance coding cells (see Methods). **f**, behavioral
1039 outcomes for one example mouse. **g**, example pairs of neurons modulated by place (yellow),
1040 time (green), or distance (orange) along with corresponding peak activity likelihood. **h**, 3D
1041 scatter plot of the distribution of cells selectively encoding a single variable along with their
1042 associated mutual information (MI) in each dimension. Cells in black either encode more than
1043 one variable or did not encode any variable significantly more than shuffled surrogates. **i**,
1044 individual traces from one example place-modulated cell (yellow) and one example time-
1045 modulated cell (green). Vertical scale bars: 1ΔF/F. **j**, tuning curves for place, time, and
1046 distance cells, sorted by the location of peak activity likelihood for each dimension (location,
1047 time, and distance). **k**, portion of total cells (log scale) encoding for one, several, or no
1048 variables. Bayesian decoding of location (**l-n**), time (**o-q**), and distance (**r-t**). For each
1049 encoded variable, posterior probabilities are plotted with the corresponding actual state (**l,o,r**).
1050 Confusion matrices between the actual vs decoded values (**m,p,s**). Decoding errors using all
1051 cells vs shuffled surrogates (**n,q,t**, left panels), spatial cells vs non spatial cells (**n**), temporal
1052 cells vs non temporal cells (**q**), distance vs non distance cells (**t**).

1053

1054 **Figure 2. Selective optogenetic pacing and ablation of theta oscillations. a**, AAV-
1055 ChrimsonR expressing vector was injected in the MS (blue, DAPI; red, ChrimsonR) and a
1056 fiber optic was placed at the injection site (white arrow). Scale bar, 1mm. **b**,

immunohistological double staining for ChrimsonR and parvalbumin (PV+) neurons. **c**, quantification of ChrimsonR+/PV+ co-expressing neurons. **d**, immunohistological double staining for ChrimsonR and cholinergic (ChAT+) neurons. **e**, quantification of ChrimsonR+/ChAT+ co-expressing neurons. **f**, recording configuration, with fiber optic in the MS and electrode in CA1. **g**, wavelet spectrograms before, during, and after scrambled (left, in red) and 8 Hz (right, in blue) stimulation patterns, with associated unfiltered LFP (white overlay, and enlarged, black traces at the bottom). **h**, average Fourier power spectra for 60 x 5s stimulation epochs (top), and sorted power spectra for each stimulation epoch (bottom) for baseline (left, in black), scrambled (center, in red), and 8 Hz (right, in blue) stimulations in a representative mouse. **i**, oscillation strength for baseline vs scrambled or 8 Hz optogenetic stimulations. Values for white noise (medium gray) and control 8 Hz sine waves are used for comparison. **j**, group average (n = 3 mice) portion of baseline power for each stimulation pattern and every frequency band (log scale). Frequency bands: δ, 1-4 Hz; θ, 4-12 Hz; α/β, 12-30 Hz; ɣslow, 30-60 Hz; ɣfast, 60-120 Hz; HFO (high frequency oscillations), 120-250 Hz.

Figure 3. GRIN lens implant does not affect theta oscillations and enables combined calcium imaging and optogenetics. a, diagram showing recording configuration (horizontal plane), with LFP electrodes in CA1 of both hemispheres, and a GRIN lens only in the right hemisphere (top). Example theta oscillations recorded in both hemispheres using wavelet spectrograms, raw (black) and theta filtered (red) traces. **b**, relative theta power measured in

1078 the right hemisphere of mice implanted with electrodes and GRIN lenses (blue) versus
1079 electrodes only (green). **c**, the relationship between miniscope LED input value and measured
1080 nominal power (purple) as well as actual light power corrected for the surface of a GRIN lens
1081 (blue). **d**, corresponding theta power from LFP electrode attached to GRIN lens when using
1082 different miniscope LED emitting light power values (in the absence of optogenetic
1083 stimulations). **e**, effects of MS optogenetic stimulations on theta oscillations during miniscope
1084 blue light emission through the lens (8AU LED power, corresponding to ~0.3mW/mm2).

1085

1086 **Figure 4. MS optogenetic stimulation modulates the activity of a subpopulation of CA1**
1087 **pyramidal cells. a**, recording CA1 neurons during MS optogenetic stimulation (5s ON, 5s
1088 OFF) while simultaneously imaging CA1 neurons in mice freely exploring an open field. **b**,
1089 peristimulus time raster plot of binarized activity for pairs of excited (left) or inhibited (right)
1090 neurons. **c**, scatter plot for all pooled neurons (n = 1849 cells, N = 5 mice) of activity
1091 probability during baseline vs stimulation (red, top: scrambled; blue, bottom: 8 Hz), for both
1092 idle (left) and running (right) periods. **d**, portion of total cells significantly modulated by
1093 stimulations (N = 5 mice). **e**, portion of modulated cells that are excited (green) or inhibited
1094 (red). **f**, spatially tuning of example neurons before (top panels) or during (bottom panels)
1095 stimulations. For the baseline condition, comparable 5 s epochs were used to sample spatial
1096 tuning (baseline A vs B). Dark blue, low activity; bright yellow, high activity. Top number
1097 indicated peak activity likelihood for each neuron. **g**, average stability of spatial tuning
1098 between stimulated and unstimulated epochs during baseline, scrambled stimulation, and 8 Hz

stimulation sessions (n = 5 mice).

Figure 5. MS optogenetic stimulation does not disrupt the stability of spatiotemporal codes. a, we recorded mice on the 3-tone linear track to identify time-, place- and distance-modulated cells (see fig. 1 and Methods). **b**, experimental timeline. **c**, spatial footprints of neurons recorded over days and comparison scheme used to assess stability (top). Example neuron (black arrow) tracked over the 5 experimental days (bottom). **d**, portion of total cells encoding for one or several (conjunctive) variables before and during 8 Hz and frequency scrambling optogenetic stimulations (N = 5 mice). **e**, sorted place fields for identified place cells across day pairs. The first day is used as a baseline and mice undergo 8 Hz, scrambled, or no stimulations (control treatment) during the other day. Stability is computed as the pairwise correlation of fields between the two-day pairs. **f**, same for time-modulated cells. **g**, same for distance-modulated cells. **h**, corresponding average stability for place-modulated cells (each dot represents a cell pooled from N = 5 mice). **i**, same for time-modulated cells. **j**, same for distance modulated cells.

Figure 6. MS optogenetic stimulation alters behavior but does not disrupt spatiotemporal codes. Using a naive Bayesian classifier, location (**a**,**b**), time elapsed (**c**,**d**), and distance traveled (**e**,**f**) were predicted from CA1 neuronal activity. **a**,**c**,**e**, decoding error (euclidean distance) for baseline, 8 Hz, and scrambled optogenetic stimulation conditions for location, time, and distance, respectively (computed in a representative mouse). **b**,**d**,**f**,

decoding z-score (higher values indicate better decoding compared to shuffled surrogate) for location, time, and distance, respectively, using N = 5 mice. **g**, example scoring of errors (purple stars) in the tone-cued linear track task. **h**, percent of correct runs during baseline, 8 Hz, and scrambled stimulations.

Figure 7. MS optogenetic stimulations disrupt maintenance and retrieval, but not encoding of episodic and working memory. a, mice were implanted with fiber optics in the MS after transfecting ChrimsonR (top). They were then subjected to the novel object place recognition task (bottom, see Methods). **b**, in this task, both scrambled (red) and 8 Hz (blue) disrupted memory performance when stimulating during the test phase. **c**, to further examine the effect of MS stimulation on memory encoding, maintenance, and retrieval, mice were trained in a delayed non-match to sample (DNMTS) task in an automated T-maze. **d**, mice were trained (in absence of stimulation) to choose the correct, non-matching arm until the performance exceeded a criterion of 0.8 portion of correct choices per day, for at least two consecutive days. **e**,**f**,**g**, performance during stimulation at different phases of the task for mice injected with ChrimonR (top) or YFP controls (bottom). Red shading indicates the stimulated regions of the maze. **e**, average daily performance when performing MS stimulations during encoding only (forced choice). **f**, average daily performance when performing MS stimulations during the 10 s delay period only. **g**, average daily performance when performing MS stimulations during the retrieval only (free choice).

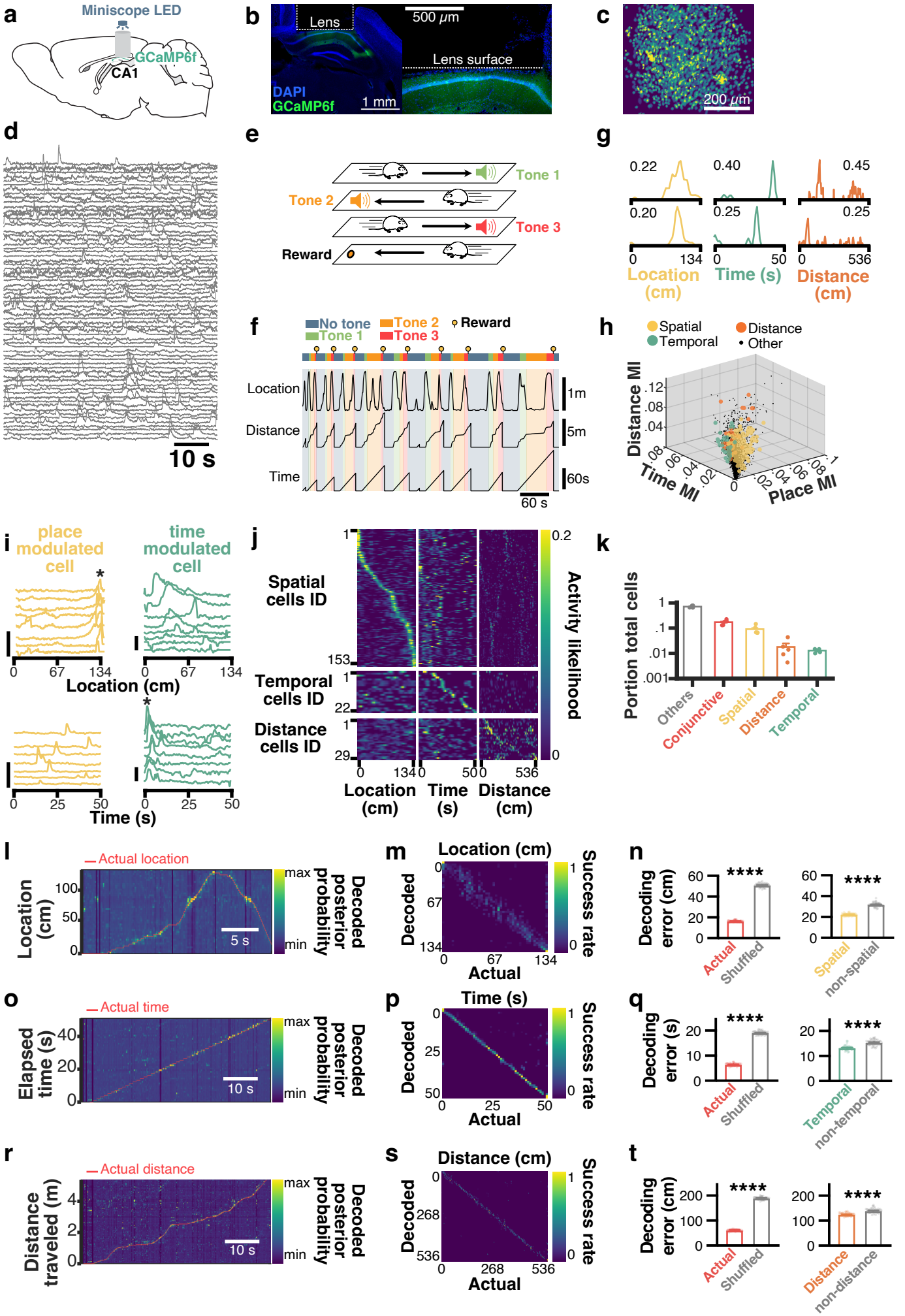
a
Miniscope LED
GCaMP6f
CA1
b
Lens
500 μm
Lens surface
DAPI
GCaMP6f
1 mm
c
200 μm
d
10 s
e
Tone 1
Tone 2
Tone 3
Reward
g
0.22
0.40
0.45
0.20
0.25
0.25
0
134
0
50
0
536
Location (cm)
Time (s)
Distance (cm)
f
No tone
Tone 1
Tone 2
Tone 3
Reward
Location
Distance
Time
1m
5m
60s
60 s
h
Spatial
Temporal
Distance
Other
Distance MI
Time MI
Place MI
i
place modulated cell
time modulated cell
Location (cm)
Time (s)
j
Spatial cells ID
Temporal cells ID
Distance cells ID
Activity likelihood
Location (cm)
Time (s)
Distance (cm)
k
Portion total cells
Others
Conjunctive
Spatial
Distance
Temporal
l
Actual location
Location (cm)
Decoded posterior probability
max
min
5 s
m
Location (cm)
Decoded
Actual
Success rate
n
Decoding error (cm)
Actual
Shuffled
Spatial
non-spatial
o
Actual time
Elapsed time (s)
10 s
p
Time (s)
q
Decoding error (s)
Temporal
non-temporal
r
Actual distance
Distance traveled (m)
s
Distance (cm)
t
Distance
non-distance

FIGURE 1

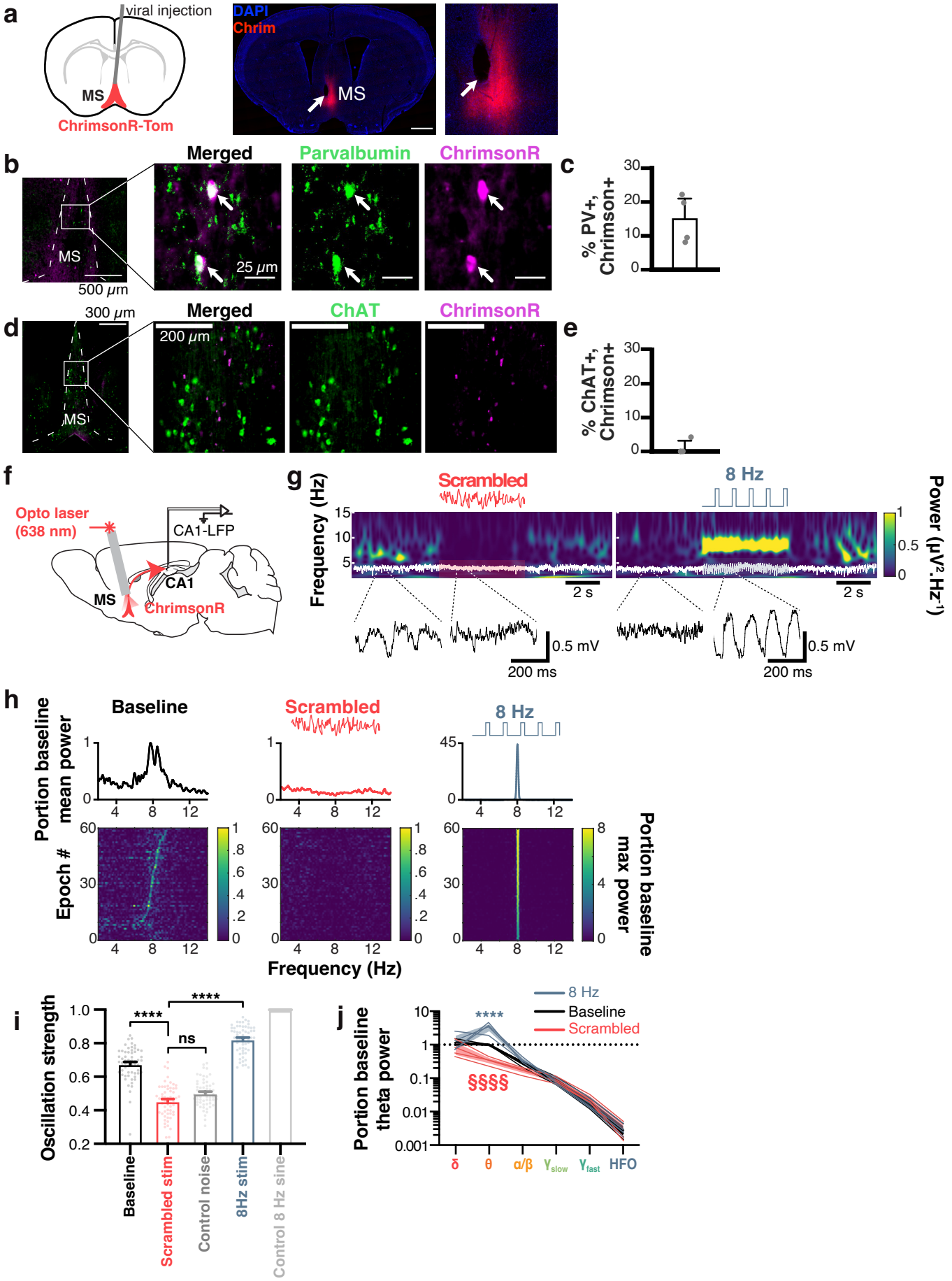
a
viral injection
MS
ChrimsonR-Tom
DAPI
Chrim
MS
b
Merged
Parvalbumin
ChrimsonR
MS
500 μm
25 μm
c
% PV+, Chrimson+
30
20
10
0
d
300 μm
Merged
ChAT
ChrimsonR
200 μm
MS
e
% ChAT+, Chrimson+
30
20
10
0
f
Opto laser (638 nm)
CA1-LFP
CA1
MS
ChrimsonR
g
Scrambled
8 Hz
Frequency (Hz)
15
10
5
2 s
0.5 mV
200 ms
Power (μV².Hz⁻¹)
1
0.5
0
h
Baseline
Scrambled
8 Hz
Portion baseline mean power
Epoch #
Portion baseline max power
Frequency (Hz)
i
Oscillation strength
1.0
0.8
0.6
0.4
0.2
****
****
ns
Baseline
Scrambled stim
Control noise
8Hz stim
Control 8 Hz sine
j
8 Hz
Baseline
Scrambled
Portion baseline theta power
10
1
0.1
0.01
0.001
****
§§§§
δ
θ
α/β
γslow
γfast
HFO

FIGURE 2

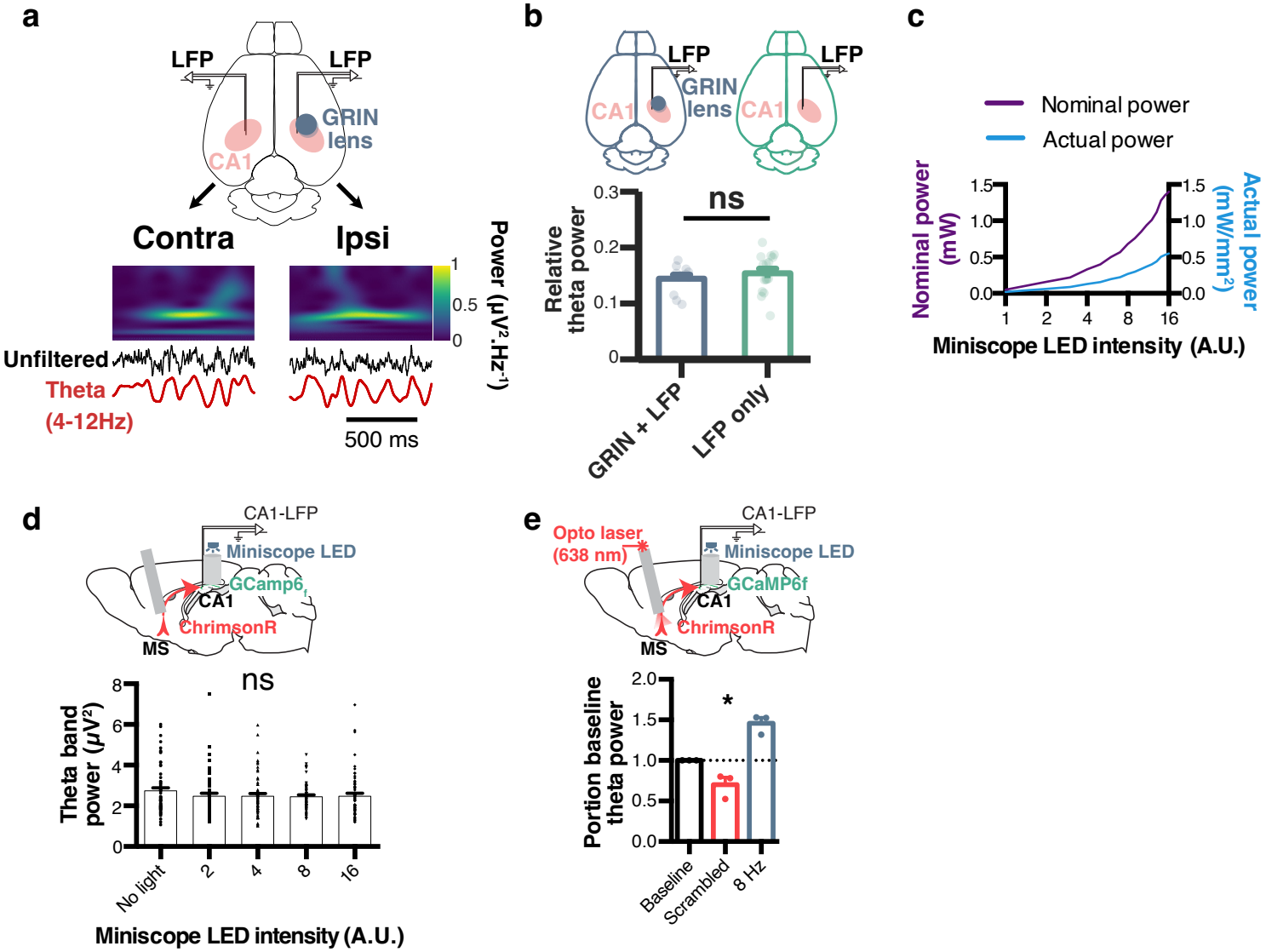
a
LFP
LFP
GRIN lens
CA1
Contra
Ipsi
Power (μV².Hz⁻¹)
1
0.5
0
Unfiltered
Theta (4-12Hz)
500 ms
b
LFP
LFP
GRIN lens
CA1
CA1
ns
Relative theta power
0.3
0.2
0.1
0
GRIN + LFP
LFP only
c
Nominal power
Actual power
Nominal power (mW)
Actual power (mW/mm²)
1.5
1.0
0.5
0.0
1
2
4
8
16
Miniscope LED intensity (A.U.)
d
CA1-LFP
Miniscope LED
GCamp6f
CA1
ChrimsonR
MS
ns
Theta band power (μV²)
8
6
4
2
0
No light
2
4
8
16
Miniscope LED intensity (A.U.)
e
Opto laser (638 nm)
CA1-LFP
Miniscope LED
GCaMP6f
CA1
ChrimsonR
MS
*
Portion baseline theta power
2.0
1.5
1.0
0.5
0.0
Baseline
Scrambled
8 Hz

FIGURE 3

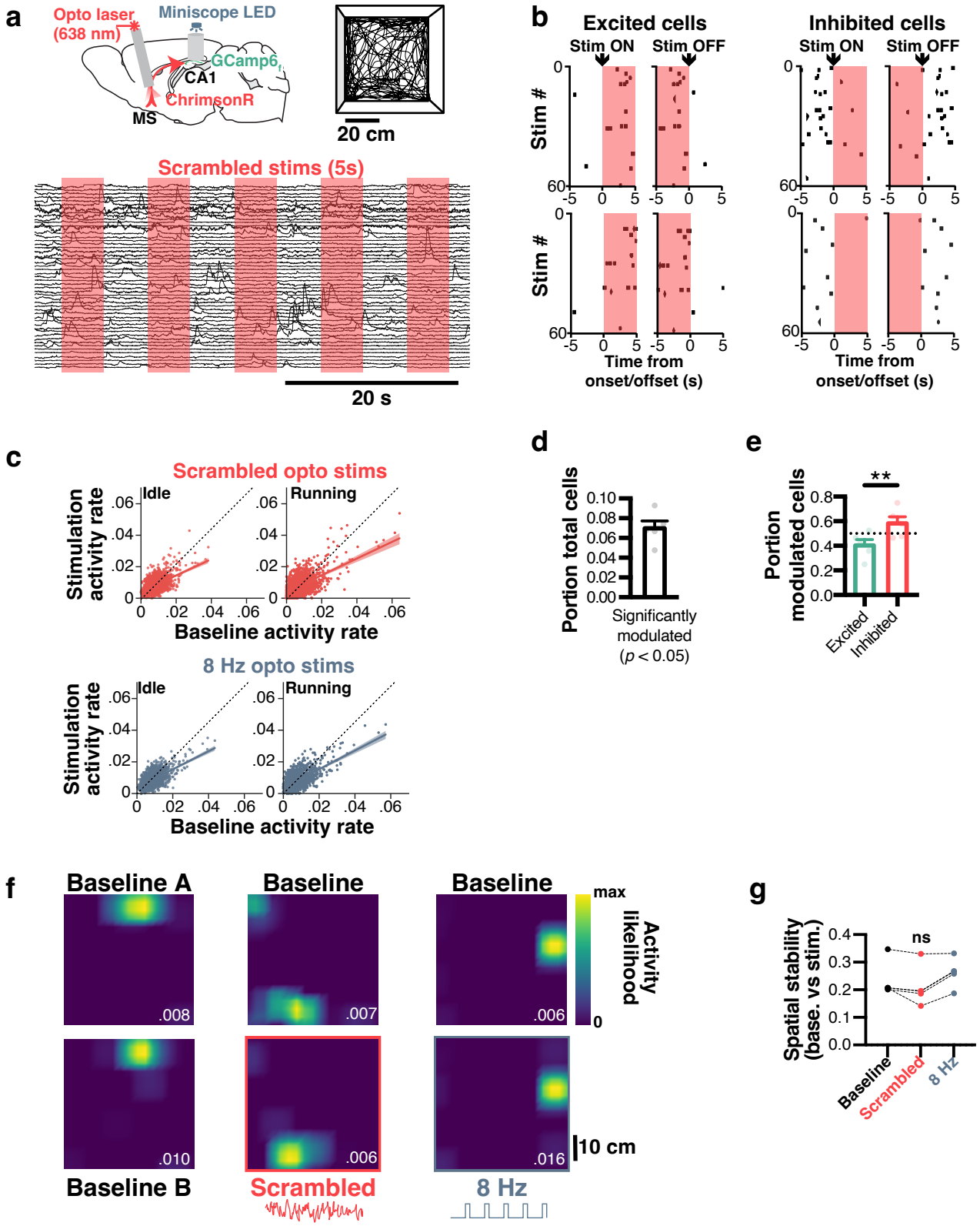
a
Opto laser (638 nm)
Miniscope LED
GCamp6
CA1
ChrimsonR
MS
20 cm
Scrambled stims (5s)
20 s
b
Excited cells
Inhibited cells
Stim ON
Stim OFF
Stim #
Time from onset/offset (s)
c
Scrambled opto stims
8 Hz opto stims
Idle
Running
Stimulation activity rate
Baseline activity rate
d
Portion total cells
Significantly modulated ($p < 0.05$)
e
Portion modulated cells
Excited
Inhibited
f
Baseline A
Baseline
Baseline
Baseline B
Scrambled
8 Hz
max
Activity likelihood
10 cm
g
Spatial stability (base. vs stim.)
ns
Baseline
Scrambled
8 Hz

FIGURE 4

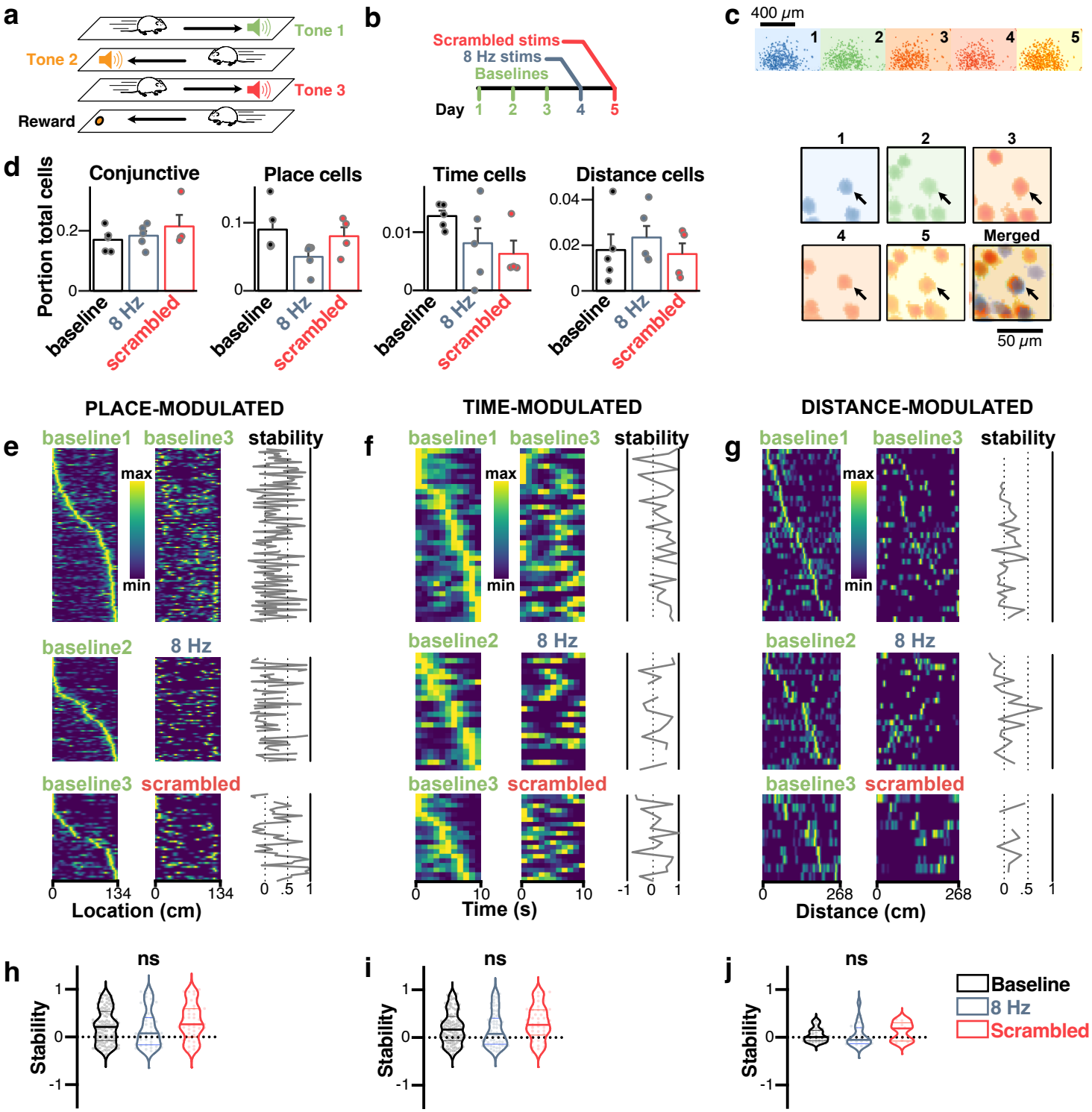
a
Tone 1
Tone 2
Tone 3
Reward
b
Scrambled stims
8 Hz stims
Baselines
Day 1 2 3 4 5
c
400 μm
1 2 3 4 5
1 2 3
4 5 Merged
50 μm
d
Portion total cells
Conjunctive
Place cells
Time cells
Distance cells
baseline
8 Hz
scrambled
PLACE-MODULATED
TIME-MODULATED
DISTANCE-MODULATED
e
f
g
baseline1
baseline3
stability
max
min
baseline2
8 Hz
baseline3
scrambled
Location (cm)
Time (s)
Distance (cm)
h
i
j
ns
Stability
Baseline
8 Hz
Scrambled

FIGURE 5

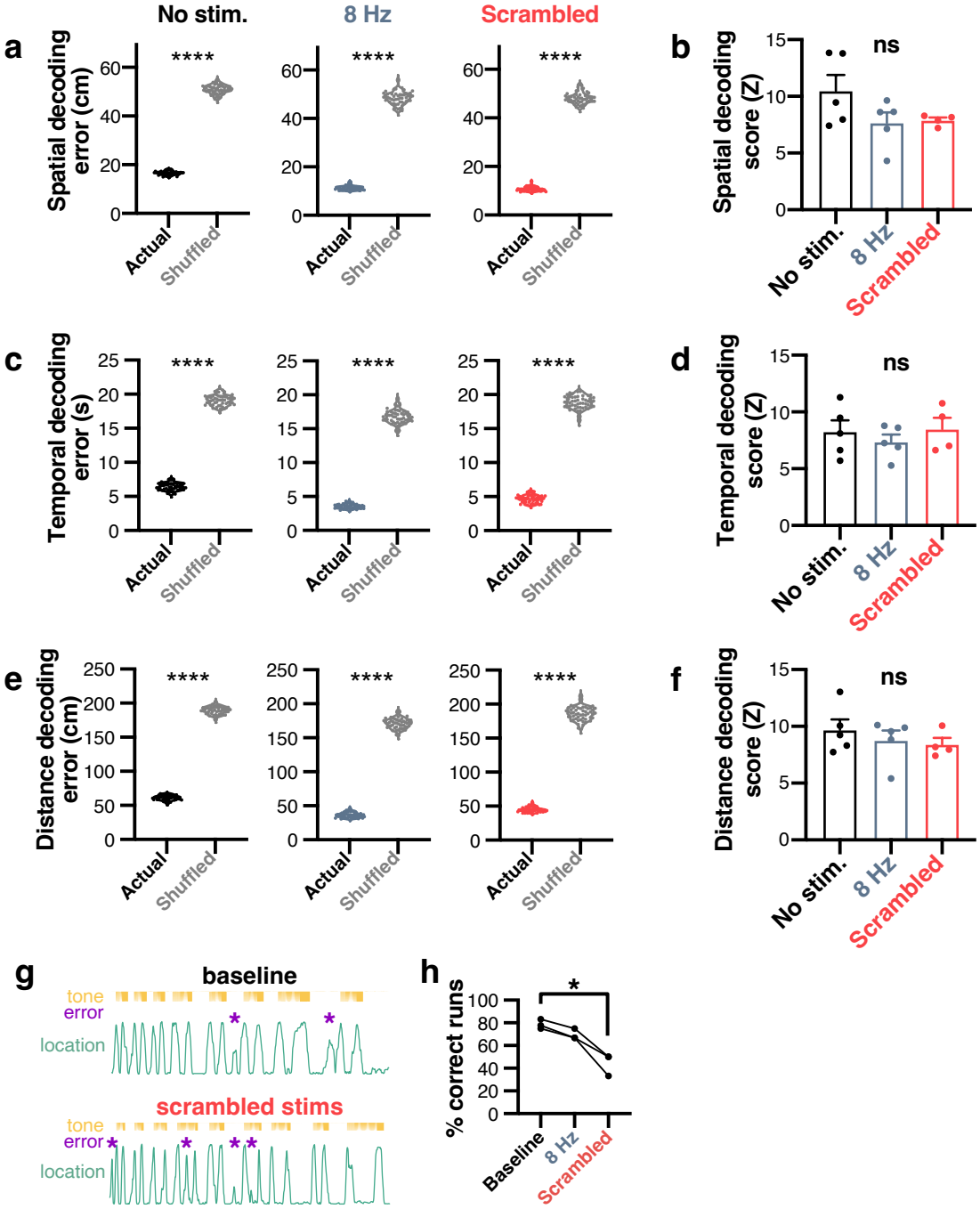
a
No stim.
8 Hz
Scrambled
Spatial decoding error (cm)
****
Actual
Shuffled
b
Spatial decoding score (Z)
ns
No stim.
8 Hz
Scrambled
c
Temporal decoding error (s)
d
Temporal decoding score (Z)
e
Distance decoding error (cm)
f
Distance decoding score (Z)
g
baseline
tone
error
location
scrambled stims
h
% correct runs
Baseline
8 Hz
Scrambled

FIGURE 6

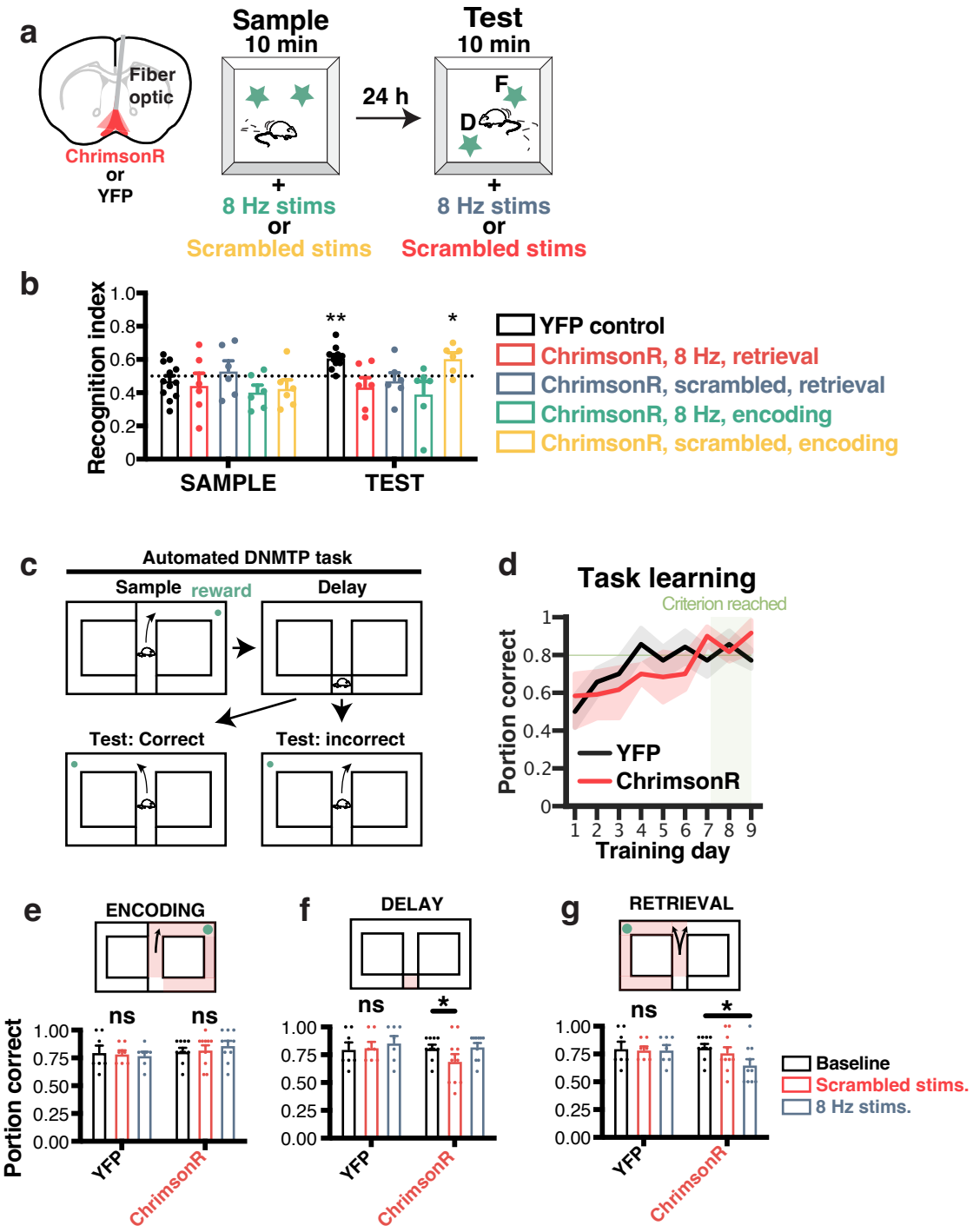
a
Fiber optic
ChrimsonR or YFP
Sample 10 min
+ 8 Hz stims or Scrambled stims
24 h
Test 10 min
F
D
+ 8 Hz stims or Scrambled stims
b
Recognition index
1.0
0.8
0.6
0.4
0.2
0
**
*
SAMPLE
TEST
YFP control
ChrimsonR, 8 Hz, retrieval
ChrimsonR, scrambled, retrieval
ChrimsonR, 8 Hz, encoding
ChrimsonR, scrambled, encoding
c
Automated DNMTP task
Sample
reward
Delay
Test: Correct
Test: incorrect
d
Task learning
Criterion reached
Portion correct
1
0.8
0.6
0.4
0.2
0
YFP
ChrimsonR
1 2 3 4 5 6 7 8 9
Training day
e
ENCODING
ns
ns
Portion correct
1.00
0.75
0.50
0.25
0.00
YFP
ChrimsonR
f
DELAY
ns
*
1.00
0.75
0.50
0.25
0.00
YFP
ChrimsonR
g
RETRIEVAL
ns
*
1.00
0.75
0.50
0.25
0.00
YFP
ChrimsonR
Baseline
Scrambled stims.
8 Hz stims.

FIGURE 7